Extraction of the proton radius from electron-proton scattering data

Gabriel Lee,[1,2,*] John R. Arrington,[3,†] and Richard J. Hill[1,‡]

[1]*Enrico Fermi Institute and Department of Physics, The University of Chicago, Chicago, Illinois 60637, USA*
[2]*Physics Department, Technion–Israel Institute of Technology, Haifa 32000, Israel*
[3]*Physics Division, Argonne National Laboratory, Argonne, Illinois 60439, USA*

We perform a new analysis of electron-proton scattering data to determine the proton electric and magnetic radii, enforcing model-independent constraints from form factor analyticity. A wide-ranging study of possible systematic effects is performed. An improved analysis is developed that rebins data taken at identical kinematic settings and avoids a scaling assumption of systematic errors with statistical errors. Employing standard models for radiative corrections, our improved analysis of the 2010 Mainz A1 Collaboration data yields a proton electric radius $r_E = 0.895(20)$ fm and magnetic radius $r_M = 0.776(38)$ fm. A similar analysis applied to world data (excluding Mainz data) implies $r_E = 0.916(24)$ fm and $r_M = 0.914(35)$ fm. The Mainz and world values of the charge radius are consistent, and a simple combination yields a value $r_E = 0.904(15)$ fm that is 4σ larger than the CREMA Collaboration muonic hydrogen determination. The Mainz and world values of the magnetic radius differ by 2.7σ, and a simple average yields $r_M = 0.851(26)$ fm. The circumstances under which published muonic hydrogen and electron scattering data could be reconciled are discussed, including a possible deficiency in the standard radiative correction model which requires further analysis.

　　　　　　PACS numbers: 13.40.Gp, 06.20.Jr, 14.20.Dh

I. INTRODUCTION

The electromagnetic form factors of the nucleons provide basic inputs to precision tests of the Standard Model and to the determination of fundamental constants [1]. These form factors are also of critical importance for the accelerator neutrino program [2]. The development of muonic atom spectroscopy [3,4] has introduced a powerful new probe of proton and nuclear structure, challenging existing results obtained from (electronic) hydrogen and electron scattering [1]. Taken at face value, in the absence of new physics explanations, the muonic hydrogen Lamb shift measurement [3] necessitates a $\gtrsim 5\sigma$ revision of the Rydberg constant, in addition to discarding or revising the predictions from a large body of previous results in both electron-proton scattering and hydrogen spectroscopy. Sources of systematic error in electron-proton scattering measurements also impact neutrino-nucleus scattering observables and hence the extraction of fundamental neutrino oscillation parameters at current and future facilities [2,5,6]. Resolution of the so-called proton radius puzzle thus has important implications across the fields of high energy, nuclear, and atomic physics [7,8].

The muonic hydrogen measurement [4] yields $r_E = 0.84087(39)$ fm, compared to $r_E = 0.8758(77)$ fm for Lamb shift measurements from ordinary (electronic) hydrogen [1]. Previous analyses of electron scattering results using the high statistics data set taken at the Mainz Microtron (MAMI) yielded [9–11] $r_E = 0.879(11)$ fm and $r_M = 0.777(19)$ fm, in both cases neglecting uncertainty associated with two-photon exchange corrections [12]. A previous global analysis of world data [13], excluding the Mainz data, yielded $r_E = 0.875(10)$ fm and $r_M = 0.867(20)$ fm. Similar results were obtained in an independent global analysis which included constraints on the large-distance behavior of an inferred proton charge distribution [14,15]. So not only are electron- and muon-based extractions of the charge radius inconsistent, but there is also a $\sim 3\sigma$ disagreement between extractions of r_M from different electron scattering data sets.

Here, we address the issue of radius extraction from electron-proton scattering data. A prominent uncertainty in the extracted radius arises from the shape of the form factor assumed when extrapolating to $q^2 = 0$ where the radius is defined in terms of the form factor slope. This can be the dominant uncertainty, as happens in particular in the A1 Collaboration's extraction of the charge radius from Mainz data [9]. In Ref. [16], one of us investigated the implications of analyticity for the form factors of electromagnetic lepton-nucleon scattering. Reference [16] considered a representative data set consisting of extracted electric form factor values from cross section data prior to 2007. In the present paper, we extend this analysis by fitting directly to cross section data, eliminating possible systematic uncertainties associated with the reduction from cross sections to form factors prior to the $q^2 \to 0$ extrapolation that defines the radius observable. We consider the most recent data, including separately a "Mainz data set" [9] and a "world data set"

[*]leeg@physics.technion.ac.il
[†]johna@anl.gov
[‡]richardhill@uchicago.edu

(defined below in Sec. IV E, excluding Mainz data). We extend the analysis of the electric form factor of the proton to consider also the magnetic form factor (see also Ref. [17]), necessary to connect with cross section data. We discuss the impact of uncertainties arising from the fitting procedure, theoretical corrections to the cross sections, and experimental systematic uncertainties. We focus here on understanding the implications of electron-proton scattering data in isolation and do not include further constraints arising from isospin decomposition in combination with electron-neutron, $\pi\pi \to N\bar{N}$, or other data [16–18]. As we will see, several critical issues in the electron scattering data demand attention before the inclusion of such further ingredients.

The remainder of the paper is structured as follows. Section II introduces notations and conventions. Section III discusses the constraints of the form factor shape arising from analyticity and perturbative scaling. Section IV reviews the status of radiative corrections and defines the default models used in the remainder of the paper. Section V analyzes the Mainz data set, employing exactly the same analysis strategy as detailed in Ref. [9], with the exception that the bounded z expansion is used in place of polynomial or spline functions to represent the form factors. Section VI studies a range of possible systematic effects. Section VII provides updated extractions of the charge and magnetic radii and uncertainties, for both the Mainz data and the world data. Section VIII presents a summary and conclusions. Supplemental Material [19] includes the data used for fits in Secs. V, VI, and VII.

II. CONVENTIONS AND NOTATION

The Dirac and Pauli form factors of the proton, F_1 and F_2, respectively, are defined by

$$\langle p(p')|J^\mu_{\text{em}}|p(p)\rangle = \bar{u}(p')\Gamma^{(p)\mu}(p', p)u(p), \quad (1)$$

where

$$\Gamma^{(p)\mu}(p', p) = \gamma^\mu F_1(q^2) + \frac{i}{2m_p}\sigma^{\mu\nu}q_\nu F_2(q^2), \quad (2)$$

with $q^\mu = p'^\mu - p^\mu$. The Sachs electric and magnetic form factors are related to the Dirac–Pauli basis by

$$G_E(q^2) = F_1(q^2) + \frac{q^2}{4m_p^2}F_2(q^2),$$

$$G_M(q^2) = F_1(q^2) + F_2(q^2), \quad (3)$$

where $G_E(0) = 1$, $G_M(0) = \mu_p \approx 2.793$ [20]. The electric and magnetic radii, r_E and r_M, are defined as the slopes of the Sachs form factors at $q^2 = 0$, i.e.,

$$\frac{G_{E,M}(q^2)}{G_{E,M}(0)} = 1 + \frac{1}{6}r_{E,M}^2 q^2 + \mathcal{O}(\alpha, q^4). \quad (4)$$

In terms of G_E and G_M, the cross section for electron-proton scattering in single photon exchange approximation is

$$\left(\frac{d\sigma}{d\Omega}\right)_0 = \left(\frac{d\sigma}{d\Omega}\right)_{\text{Mott}} \frac{\epsilon G_E^2 + \tau G_M^2}{\epsilon(1 + \tau)}, \quad (5)$$

where $(d\sigma/d\Omega)_{\text{Mott}}$ is the recoil-corrected relativistic point particle (Mott) result,

$$\left(\frac{d\sigma}{d\Omega}\right)_{\text{Mott}} = \frac{\alpha^2}{4E^2 \sin^4\frac{\theta}{2}}\frac{E'}{E}\cos^2\frac{\theta}{2}. \quad (6)$$

Here, $Q^2 = -q^2$, E is the initial electron energy, $E' = E/[1 + (2E/m_p)\sin^2(\theta/2)]$ and θ are the energy and angle with respect to the beam direction of the final state electron, and ϵ, τ are the dimensionless kinematic variables

$$\tau = \frac{Q^2}{4m_p^2}, \qquad \epsilon = \left[1 + 2(1 + \tau)\tan^2\frac{\theta}{2}\right]^{-1}. \quad (7)$$

In fits to the Mainz data below, we employ the beam energy E and the acceptance-averaged Q^2 as independent variables, as dictated by the presentation of experimental results in this data set. In fits to world data excluding Mainz data, we employ E and θ.

III. FORM FACTOR SHAPE

When performing statistical analyses that constrain the form factors and derived quantities such as the radius, it is important that the class of allowed functions be large enough to contain the true form factors but sufficiently constrained for meaningful values to be obtained, i.e., without arbitrarily large errors, and such that overfitting to statistical noise does not bias parameter extractions. We summarize here our knowledge about the analytic structure of the form factors, introduce notation for the z expansion, and explain an important property of the z expansion with regard to convexity and stability of fits involving many parameters.

A. Analyticity and z expansion

Let us recall the analytic structure of the form factors $F_1(q^2)$, $F_2(q^2)$, or equivalently $G_E(q^2)$, $G_M(q^2)$. The form factors may be extended to functions of the complex variable $t = q^2$, analytic outside of a cut at timelike values of t, beginning at the two-pion production threshold, $t \geq 4m_\pi^2$.[1] In the restricted kinematic region accessed in a given experimental data set, $-Q_{\text{max}}^2 \leq t \leq 0$, the finite

---

[1]Here and throughout, $m_\pi = 140$ MeV denotes the charged pion mass. Accounting for isospin violation would imply a smaller threshold at $4m_{\pi^0}^2$. A conservative approach to accounting for this effect would be to lower the threshold; we have verified that the difference is inconsequential to the fits.

distance to singularities implies the existence of a small expansion parameter, $|z|_{max} < 1$. To see this, we perform a conformal mapping of the domain of analyticity onto the unit circle,[2]

$$z(t, t_{cut}, t_0) = \frac{\sqrt{t_{cut} - t} - \sqrt{t_{cut} - t_0}}{\sqrt{t_{cut} - t} + \sqrt{t_{cut} - t_0}}, \qquad (8)$$

where $t_{cut} = 4m_\pi^2$ and t_0 is a free parameter representing the point mapping onto $z = 0$. By the "optimal" choice $t_0^{opt}(Q_{max}^2) = t_{cut}(1 - \sqrt{1 + Q_{max}^2/t_{cut}})$, the maximum value of $|z|$ is minimized: $|z| \leq |z|_{max}^{opt} = [(1 + Q_{max}^2/t_{cut})^{\frac{1}{4}} - 1]/[(1 + Q_{max}^2/t_{cut})^{\frac{1}{4}} + 1]$. For example, with $Q_{max}^2 = 0.05, 0.5$, and 1 GeV^2, we have $|z|_{max}^{opt} \approx 0.06, 0.25$, and 0.32, respectively.[3] Expanding the form factors as

$$G_E(q^2) = \sum_{k=0}^{k_{max}} a_k z^k, \qquad G_M(q^2) = \sum_{k=0}^{k_{max}} b_k z^k, \quad (9)$$

we find that higher-order terms are suppressed by powers of this small parameter.

B. Coefficient bounds and large-k scaling

The identity [5],

$$\sum_{k=0}^{\infty} a_k^2 = \frac{1}{\pi} \int_{t_{cut}}^{\infty} \frac{dt}{t - t_0} \sqrt{\frac{t_{cut} - t_0}{t - t_{cut}}} |G|^2 < \infty, \qquad (10)$$

ensures that the coefficients multiplying z^k are not only bounded in size but must decrease at large k. This guarantees that a finite number of parameters is necessary to describe the form factor with a given precision throughout the kinematic region of interest. In the fits performed in this paper, we focus on the class of form factors (9), with a uniform bound on $|a_k/a_0|$ and $|b_k/b_0|$. A study of form factor models, explicit spectral functions, and scattering data motivates the conservative bound of $|a_k/a_0|_{max} = |b_k/b_0|_{max} = 5$ for either $t_0 = 0$ or $t_0 = t_0^{opt}$ when limiting the fit to $Q_{max}^2 \approx 1$ GeV^2 [5,17]. We adopt this bound for our default fits but study also the case of modified bounds.

In fact, a stronger statement can be made regarding the large-k behavior of the expansion coefficients. Since at large spacelike values of momentum transfer, $Q^2 \to \infty$, the Sachs form factors are known to fall as $1/Q^4$ up to logarithms [22], we have that $Q^k G(-Q^2) \to 0$, $k = 0, ..., 3$. From Eq. (9), this implies

$$\left. \frac{d^n}{dz^n} G_E \right|_{z=1} = 0, \qquad n = 0, 1, 2, 3, \qquad (11)$$

or, equivalently, the series of four sum rules,

$$\sum_{k=n}^{\infty} k(k-1) \cdots (k - n + 1) a_k = 0, \qquad n = 0, 1, 2, 3.$$

$$(12)$$

Absolute convergence of these series corresponds to $a_k = \mathcal{O}(1/k^4)$.[4]

C. Convexity and χ^2 minimization

An important feature of Taylor expanded amplitudes facilitates efficient and stable numerical fits.[5] Consider a χ^2 function of schematic form

$$\chi^2 = \sum_i \frac{(A_i^2 - M_i)^2}{E_i^2}, \qquad A_i = \sum_n a_n x_i^n, \qquad (13)$$

where the sum is over data points labeled by index i, M represents a measurement, E is the error on the measurement, and A is the theoretical amplitude expressed in terms of a kinematic variable x [e.g., $x_i = z(q_i^2)$ in the present application]. The Taylor expansion coefficients a_n are fit parameters to be determined by minimizing χ^2.

If $\chi^2(\{a_n\})$ is a convex function of its arguments, a_n, then any local minimum is necessarily a global minimum, and the relevant optimization problem is amenable to efficient numerical algorithms. In general, determining convexity of a multivariate quartic polynomial is NP hard [23]. We notice, however, that the matrix of second derivatives is

$$\frac{\partial^2 \chi^2}{\partial a_n \partial a_m} = 4 \sum_i x_i^{n+m} \left(\frac{3A_i^2 - M_i}{E_i^2} \right). \qquad (14)$$

Each term in the sum over i is seen to be a positive semidefinite matrix provided that amplitudes satisfy $3A_i^2 > M_i$. Each contribution in Eq. (13) is thus convex throughout the parameter regime where this physical condition is satisfied. Since a linear combination of convex polynomials with positive coefficients is convex, the sum of terms in Eq. (13) is also convex in this regime. It is thus straightforward to build up solutions to the numerical χ^2 minimization problem over a large number of parameters by successively increasing the number of parameters and data points, using the previous solution $\{a_n\}$ as the initial condition. The convexity condition ensures that this

---

[2]For a discussion and further references, see Ref. [21].
[3]For $t_0 = 0$, these numbers become approximately twice as large, $|z|_{max} \approx 0.12, 0.46$, and 0.58.

[4]Absolute convergence may be verified by inspecting the analog of Eq. (10) applied to $|d^n G/dz^n|^2$ in place of $|G|^2$.
[5]While this observation has emerged from a particular example of fits to electron scattering data, the argument applies to general quantum mechanical observables represented as squares of Taylor-expanded amplitudes.

procedure does not yield a solution that is a local but not a global minimum.

The preceding arguments strictly apply when a single form factor dominates, which is, for example, the case for G_E in Eq. (5) at low Q^2. In the general case in which G_E and G_M are fit simultaneously, the χ^2 function takes a more general form involving the sum of probabilities, $A_i^2 \rightarrow A_i^2 + B_i^2$, for which the simple convexity theorem following from Eq. (14) no longer applies. It may be interesting to pursue more general "physical convexity" theorems involving multiple probability sums and correlated errors.

D. Advantages over other parametrizations

We remark that several parametrizations of the proton form factors in common use rely on somewhat arbitrary expansions. A simple Taylor expansion in q^2 [24] is only guaranteed to converge below the pion production threshold $q^2 \leq 4m_\pi^2 \approx 0.08$ GeV^2. Convergence of a sequence of Padé approximants, implemented either directly as a ratio of polynomials [25,26] or as a continued fraction [27,28], requires positivity of the spectral function in the dispersive representations of the form factors, a property which is not satisfied.[6]

While these functions may be able to provide a sufficiently precise representation of the form factors with enough fit parameters, the parameters tend to be highly correlated. Without any way to bound the parameters, these correlations can lead to a large uncertainty on any given parameter (such as the radius) that grows as the number of parameters increases. Because of this, it may be difficult or impossible to include enough parameters to properly reproduce the data while at the same time achieving a meaningful limit on the extracted radius. The correlation between different parameters may also lead to the situation in which overfitting the noise in data at high Q^2 biases the extracted radius. This concern applies especially for the magnetic form factor for which the data at low Q^2 have larger uncertainties than the higher Q^2 data.

IV. RADIATIVE CORRECTIONS

In this section, we provide a brief summary of one-loop radiative corrections and Sudakov resummation in electron-proton scattering. We extract the radius according to Eq. (4), using data to which corrections have been applied to extract a Born cross section. To understand the impact of the different corrections applied to various data sets, we begin in Secs. IV A–IV D with a brief overview of notation and results for one-photon exchange, two-photon exchange, real photon emission, and Sudakov resummation as they impact cross section measurements. In Sec. IV E,

we return to a discussion of experimental implementations for the data sets employed in the remainder of this paper.

A. One-photon exchange

The (on-shell, renormalized) scattering amplitude for the electron-proton scattering process $e(k)p(p) \rightarrow e(k')p(p')$ involving one exchanged photon may be written

$$\mathcal{M}_1 = -\frac{4\pi\alpha}{q^2} \frac{1}{1 - \hat{\Pi}(q^2)} \bar{u}^{(e)}(k') \Gamma^{(e)\mu}(k', k) u^{(e)}(k)$$
$$\times \bar{u}^{(p)}(p') \Gamma^{(p)}_\mu(p', p) u^{(p)}(p) \quad (15)$$

and includes radiative corrections involving the proton and electron vertices (and wave function renormalization) and vacuum polarization. Here, $\alpha = 7.297 \times 10^{-3}$ is the fine structure constant. The proton vertex function $\Gamma^{(p)}(p', p)$ is expressed, as in Eq. (2), in terms of the IR divergent on-shell form factors discussed below. The electron vertex function $\Gamma^{(e)}(k', k)$ is similarly expressed in terms of on-shell form factors normalized as $F_1^{(e)}(0) \equiv 1$, $F_2^{(e)}(0) \equiv a_e \approx \alpha/(2\pi)$. The photon propagator correction $\hat{\Pi}(q^2)$ accounts for contributions of both leptonic and hadronic vacuum polarization.

The on-shell form factors appearing in Eq. (15) are necessarily infrared divergent at nonzero momentum transfer, as deduced by the cancellation with bremsstrahlung emission. In terms of a photon mass, let us introduce conventional "Born" form factors which are finite including first-order radiative effects in the $\lambda \rightarrow 0$ limit. We employ the tilde notation $\tilde{F}_i$ to denote the on-shell form factor with the corresponding Born form factor F_i:

$$\tilde{F}_i(q^2) \equiv \left\{ 1 - \frac{\alpha}{2\pi} [K(p, p') - K(p, p)] \right\} F_i(q^2). \quad (16)$$

Here, $K(p_1, p_2)$ denotes the integral [29,30]

$$K(p_1, p_2) = \frac{2p_1 \cdot p_2}{-i\pi^2} \int d^4L \frac{1}{L^2 - \lambda^2 + i0}$$
$$\times \frac{1}{L^2 + 2L \cdot p_1 + i0} \frac{1}{L^2 + 2L \cdot p_2 + i0} \quad (17)$$

and is readily evaluated in analytic form. The electric and magnetic radii are now defined as the slopes of the Born form factors with respect to q^2,

$$\frac{G'_{E,M}(0)}{G_{E,M}(0)} = \frac{1}{6} r^2_{E,M}. \quad (18)$$

Infrared divergences are absorbed into the extracted prefactors in Eq. (16) and will cancel upon including the effects of real photon emission. The electron form factors may be calculated analytically in QED, with infrared

---

[6]That it cannot be satisfied is readily seen from the asymptotic behavior Q^{-2} for the form factor represented by such a spectral function.

divergences similarly cancelling against real emission. For completeness, let us note that for the IR divergent on-shell Sachs form factors we have

$$\frac{\tilde{G}'_{E,M}(0)}{\tilde{G}_{E,M}(0)} \equiv \frac{1}{6} r^2_{E,M} + \frac{\alpha}{3\pi m_p^2}\left(\log\frac{m_p}{\lambda} + \frac{1}{4}\right). \quad (19)$$

Leptonic vacuum polarization contributions to $\hat{\Pi}(q^2)$ are readily computed analytically, and the hadronic contributions are constrained by $e^+e^- \to$ hadrons data.[7] For the purposes of determining the radii, we may simply absorb the hadronic contribution $\hat{\Pi}_{had}(q^2)$ into an alternate definition of the reduced form factors:

$$F_i(q^2) \to [1 - \hat{\Pi}_{had}(q^2)]^{-1} F_i(q^2). \quad (20)$$

Several remarks are in order. First, we note that Eq. (16) is not a *calculation* of proton-vertex radiative corrections but rather a *definition* of Born form factors in the presence of radiative corrections. The definitions of the radii following from Eqs. (16) and (18) differ slightly from the definition of Maximon and Tjon [30] which includes an additional contribution (there denoted $\delta^{(1)}_{el}$) involving a sticking-in-form-factors (SIFF) ansatz for the proton vertex. However, in many analyses (including, in particular, Ref. [9]), the additional contributions beyond those in Eq. (16) are anyways ignored. The convention (16) does not require the specification of a form factor model and is closely aligned with standard treatments of electron scattering. Let us further remark that this convention differs slightly from a convention commonly used in atomic physics applications [32]. However, the difference, represented by the term $\alpha/(12\pi m_p^2)$ in Eq. (19), corresponds to a relative shift of $\sim 2 \times 10^{-5}$ in r_E, well below current experimental sensitivities in either electron scattering or muonic hydrogen.

Second, we remark that if hadronic vacuum polarization is not removed explicitly before fitting then the resulting proton form factors should be interpreted with the alternate definition (20). With this definition, the fitted radius now corresponds to

$$[r^2_{E,M}]^{fit} = r^2_{E,M} + 6\hat{\Pi}'_{had}(0). \quad (21)$$

A dispersive analysis of $e^+e^- \to$ hadrons data yields [33,34],

$$\hat{\Pi}'_{had}(0) = -9.31(20) \times 10^{-3} \text{ GeV}^{-2}. \quad (22)$$

This correction leads to a small shift, ~ 0.001 fm, in r_E, and a more careful error analysis does not appear to be

warranted at the current level of precision. We note that Ref. [9] did not account for hadronic vacuum polarization explicitly and hence implicitly employed the alternate definition (20). Experiments in the world data set used explicit models to account for hadronic vacuum polarization or included uncertainties to account for the neglect of this correction. Hence, the extracted radii should differ slightly from the Mainz value according to the replacement (21), but the effect is well below the current experimental precision.[8] The treatment in Eq. (20) efficiently accounts for the effects of hadronic vacuum polarization on the radii in terms of the single number $\hat{\Pi}'_{had}(0)$. When interpreting form factors at finite momentum transfer, care must be taken to account for the q^2 dependence of hadronic vacuum polarization.

Finally, we note that the analytic structures of the functions $K(p, p')$ in Eq. (16) and of $\hat{\Pi}_{had}(q^2)$ in Eq. (20) do not upset the assumptions going into the z expansion, since these functions are analytic outside of a cut at timelike $q^2 \geq 4m_p^2$ for $K(p, p')$ and at $q^2 \geq 4m_\pi^2$ for $\hat{\Pi}_{had}(q^2)$.

B. Two-photon exchange

The two-photon exchange (TPE) contribution may be written

$$\begin{aligned}\mathcal{M}_2 &= \frac{\alpha}{2\pi}[-K(p,-k) - K(p',-k') + K(p,k') \\ &\quad + K(p',k)]\mathcal{M}_1 + \hat{\mathcal{M}}_2^{MoTs} \\ &= \frac{\alpha}{\pi}\left[-\frac{E}{\sqrt{E^2 - m_e^2}}\log\left(\frac{E + \sqrt{E^2 - m_e^2}}{m_e}\right)\right. \\ &\quad \left. + \frac{E'}{\sqrt{E'^2 - m_e^2}}\log\left(\frac{E' + \sqrt{E'^2 - m_e^2}}{m_e}\right)\right] \\ &\quad \times \log\frac{Q^2}{\lambda^2}\mathcal{M}_1 + \hat{\mathcal{M}}_2^{MaTj}. \end{aligned} \quad (23)$$

The $K(p_1, p_2)$ functions are defined above in Eq. (17). As indicated in Eq. (23), two conventions exist in the literature for isolating an IR finite TPE contribution: $\hat{\mathcal{M}}_2^{MoTs}$ [29] (Mo-Tsai) and $\hat{\mathcal{M}}_2^{MaTj}$ [30] (Maximon-Tjon). As long as the full correction $\mathcal{M}_2$ is applied to the data, the results are independent of the convention used to separate IR divergent and IR finite contributions. Our hadronic model for the finite contribution is based on the Maximon–Tjon convention and so yields the complete $\mathcal{M}_2$ when applied to the

---

[7]Alternatively, one could model the hadronic contributions by quark loop diagrams [31]; however, strong interaction corrections are not controlled at small $Q^2 \lesssim \Lambda_{QCD}^2$.

[8]An explicit correction for hadronic vacuum polarization is typically applied in atomic physics analyses. This is the case in particular for the CREMA analysis of muonic hydrogen [3]. To avoid a double counting, the shift (21) should therefore in principle be applied to electron scattering extractions that absorb this correction into the definition of the radius, before input or comparison to atomic physics extractions.

Mainz data, which uses the same convention. For the world data, the Mo-Tsai convention is used, and so our calculation of $\hat{\mathcal{M}}_2^{\mathrm{MaTj}}$ yields a total $\mathcal{M}_2$ contribution that differs by -0.4% to 0.1% at the cross section level compared to the consistent combination. This small error is accounted for in the radiative correction uncertainties quoted for these measurements, and we have verified that such differences have an insignificant impact on the extracted radii.

As a default, we employ the SIFF ansatz to estimate the TPE correction [35–38]. We have computed $\mathcal{M}_2$ using two form factor models. The first uses dipole F_1, F_2 form factors,

$$F_{1,2}(q^2) \to F_{1,2}(0)\left(1 - \frac{q^2}{\Lambda^2}\right)^{-2}, \qquad (24)$$

with a value $\Lambda^2 = 0.71~\mathrm{GeV}^2$. The second model represents F_1, F_2 as a sum of monopoles,

$$F_{1,2}(q^2) \to \sum_{j=1}^{N} \frac{n_j}{d_j - q^2}. \qquad (25)$$

To compare with previous results in the literature [35], we consider in particular the case $N = 3$ with parameter values n_j, d_j given in Table I. We compare these models for $\mathcal{M}_2$ to results with vanishing finite TPE correction in the Maximon-Tjon convention,

$$\hat{\mathcal{M}}_2^{\mathrm{MaTj}}(\text{no TPE}) = 0, \qquad (26)$$

and to results setting $\hat{\mathcal{M}}_2^{\mathrm{MaTj}}/\mathcal{M}_1$ equal to the complete, "Feshbach" [39], result for $\mathcal{M}_2/\mathcal{M}_1$ in the $m_p \to \infty$ limit[9]:

$$\hat{\mathcal{M}}_2^{\mathrm{MaTj}}(\text{Feshbach}) = \left(1 + \pi\alpha\frac{\sin\frac{\theta}{2}}{1 + \sin\frac{\theta}{2}}\right)\mathcal{M}_1. \qquad (27)$$

C. Soft bremsstrahlung

The soft bremsstrahlung contribution to the cross section is

$$d\sigma_{\mathrm{brem}} = -\frac{\alpha}{4\pi^2}d\sigma_0 \int \left.\frac{d^3\ell}{\sqrt{\ell^2 + \lambda^2}}\right|_{|\vec{\ell}| \leq (E/E')\Delta E}$$
$$\times \left(\frac{k'}{k'\cdot\ell} - \frac{k}{k\cdot\ell} - \frac{p'}{p'\cdot\ell} + \frac{p}{p\cdot\ell}\right)^2, \qquad (28)$$

---

[9]An imaginary part in Eq. (27) is ignored since it affects the cross section only at relative order α^2. For definiteness, we have expressed the result in terms of (E, θ) instead of the variables (E, Q^2) before taking the $m_p \to \infty$ limit, to match the expression used in Ref. [9].

TABLE I. Expansion coefficients for Eq. (25) in the SIFF TPE prescription of Ref. [35]. Note that n_3 is determined by $F_{1,2}(0) = \sum_j n_j/d_j$.

	F_1	F_2
n_1	0.38676	1.01650
n_2	0.53222	−19.0246
d_1	3.29899	0.40886
d_2	0.45614	2.94311
d_3	3.32682	3.12550

where ΔE is the accepted energy cut interval for the final state electron in the lab frame. This integral may be evaluated analytically [30]. After cancellation of infrared divergences, the differential cross section including first-order real and virtual radiative effects may be written

$$d\sigma = (d\sigma)_0(1 + \delta). \qquad (29)$$

Here, $(d\sigma)_0$ is the cross section (5), expressed in terms of Born form factors, and δ is a finite correction depending on kinematic variables that accounts for vertex, vacuum polarization, and TPE radiative corrections.

D. Large log resummation

The preceding subsections (Secs. IV A–IV C) summarize a complete treatment of first-order radiative corrections. The hadronic input, apart from the form factors to be determined, consists of a TPE model for $\hat{\mathcal{M}}_2$ in Eq. (23) and the number $\hat{\Pi}'_{\mathrm{had}}(0)$ (the latter impacts the radius at a level below current uncertainties). However, we wish to describe scattering data with momentum transfers as large as $Q^2 \sim 1~\mathrm{GeV}^2$. In this regime, large logarithms from electron radiative corrections cause a poor convergence, or even breakdown, of the naive perturbation theory, since

$$\left.\frac{\alpha}{\pi}\log^2\frac{Q^2}{m_e^2}\right|_{Q^2 \sim 1~\mathrm{GeV}^2} \approx 0.5. \qquad (30)$$

Thus, first-order radiative corrections are insufficient for percent-level accuracy.

When $Q \sim E \sim E'$ and $m_e \sim \Delta E$, the leading series of logarithms $\alpha^n \log^{2n}(Q^2/m_e^2)$ are resummed by making in (29) the replacement,

$$1 + \delta \to \exp(\delta). \qquad (31)$$

Two-loop corrections without logarithmic enhancement are below the relevant experimental precision. For definiteness, in our analysis of the Mainz data, we employ the prescription used in Ref. [9], exponentiating all first-order corrections in (31) except the finite TPE contributions. We return to a discussion of deficiencies in this treatment in Sec. VII C 3.

E. Summary of experimental implementations

Apart from TPE and, in some cases, large log resummation, radiative corrections have already been applied to all of the cross sections we include in our fit, as part of the original analysis of the experiments. We will examine the impact of different TPE prescriptions, with final results based on the SIFF sum of monopoles TPE correction as in Eq. (25) and Table I. Possible deficiencies in radiative corrections are treated at the same level as experimental systematic errors.

Consider first the Mainz data set. The A1 Collaboration's data analysis applied radiative corrections based on the prescription of Refs. [30,40], as detailed in Ref. [9]. This includes TPE corrections using the Feshbach prescription [39] and the large log resummation given in Eq. (31) above (excluding the finite TPE contribution from the exponentiation). In the analysis of correlated systematic uncertainties, the cutoff on the bremsstrahlung tail was varied, yielding rms cross section variations well below 0.1%. These variations in the cross sections were used to determine the impact of radiative correction uncertainties on the radius. No uncertainty was included in the cross sections for the TPE contribution.

Consider now the world data set. The world data come from many different experiments, and the details of the radiative corrections vary. However, they are all based on the general formalism of Mo and Tsai [29,41,42], with improvements and modifications added in later works, e.g., Refs. [31,43]. Our compilation of world data comes from Ref. [44], along with additional low Q^2 and more recent cross section [45–48] and recoil polarization or polarized target measurements [13,49–56], with earlier polarization transfer results [57–59] replaced by the results of final, updated analyses [60–62]. Further details of radiative corrections, in particular for earlier experiments, are presented in Ref. [63]. Our compilation includes the corrections applied to earlier measurements discussed in that work; furthermore, we include additional vacuum polarization terms, exclude small angle data, $\theta < 20°$, from Ref. [43], and include separate normalization factors for data taken with different detectors or under very different conditions [64–66].

The original publications of the experiments comprising the world data set did not apply TPE corrections, and different prescriptions were used to approximate Eq. (31). For the most part, these experiments quoted normalization and uncorrelated uncertainties of 0.5%–1% each to account for uncertainties in the radiative corrections applied, dominated by uncertainty associated with TPE corrections.[10] In this case, we will apply TPE corrections similar to those applied in the previous global analysis [26], for which the errors assigned in previous experiments were taken to be sufficient to account for uncertainties after applying a hadronic calculation of the TPE corrections. Note that one experiment [68] did not include uncertainties associated with these corrections and so had much smaller total uncertainties than other experiments. Following Ref. [26], we thus include an additional systematic uncertainty to the data of Ref. [68]: we increase the normalization uncertainty by 1% (to a total of 1.5%) and add 0.5% in quadrature to the point-to-point uncertainty.

In Sec. VII, we will include constraints on the form factor ratio G_E/G_M from polarization measurements. In the kinematic range considered, with $Q^2 \leq 1$ GeV^2, the TPE correction, estimated from a simple hadronic model [35], is small compared to experimental errors.[11] Following Ref. [26], this model-dependent correction is thus omitted from the fits. We will find that the polarization data points do not have a strong influence on the radius fits and thus do not pursue a more detailed treatment of radiative corrections to these data points.

V. UPDATED FIT OF THE MAINZ DATA SET

In this section, we extract the charge and magnetic radii from the Mainz data set, retaining the original treatment of statistical and systematic uncertainties and correction factors from Ref. [9] but incorporating our knowledge of the structure of the form factors as presented in Sec. III. We first reproduce the Mainz polynomial and inverse polynomial fits and then provide an updated extraction using the bounded z expansion. To highlight differences in the theoretical treatment of the form factors, we fit to the full data set (1422 points) and apply the Feshbach correction as the only TPE correction, as was done in the primary radius extraction from Ref. [9]. We then discuss the impact of moving from polynomial fits to fits using the bounded z expansion and comment on other attempts to extract the radii from the Mainz data.

Note that, because of the way the data and uncertainties are parametrized for the Mainz data, the uncertainties from such a fit represent only part of the total uncertainty. Meaningful error estimates require the examination of correlated effects arising, e.g., from experimental systematic errors and radiative corrections. In this section, we focus on how the improved form factor parametrization modifies the extracted radii and fit uncertainties. Section VI will include an examination of the corrections applied to the Mainz data and the treatment of systematic uncertainties presented in their analysis.

---

[10]While this turned out to be smaller than the size of TPE corrections in recent calculations [37,38], it appears to be a significant overestimate of the residual uncertainty at lower Q^2 values, based on the consistency between low-Q^2 estimates of the corrections [67].

[11]The hadronic model for TPE corrections [35] predicts a correction not larger than $\sim 0.5\%$ over the full ϵ range for $Q^2 \leq 1$ GeV^2. Furthermore, the 41 data points with $Q^2 \leq 1$ GeV^2 are concentrated at large epsilon, $\epsilon \approx 0.7 \pm 0.2$, where the TPE correction model predicts a correction $\lesssim 0.2\%$.

We take the cross section data as provided in the Supplemental Material of Ref. [9], which includes the Feshbach correction for TPE, and scaling of the statistical uncertainties to account for unidentified systematic errors, as discussed in Sec. VI. We allow the normalization parameters to float freely in the fit, in accordance with Ref. [9]. In addition to examining the full Mainz data set, we also provide results obtained by restricting to momentum transfers below a given Q^2_{max}. We use the χ^2 function

$$\chi^2_\sigma = \sum_{i=1}^{N_\sigma} \frac{(\sigma_i - \sigma_{i,\text{fit}}/\eta_{i,\text{fit}})^2}{\delta\sigma_i^2}. \qquad (32)$$

Here, N_σ is the number of cross section points for a specified kinematic cut Q^2_{max}, σ is the measured cross section (after accounting for radiative corrections), $\delta\sigma$ is the (point-to-point, uncorrelated) uncertainty, σ_{fit} is the cross section calculated using the chosen form factor model, and η_{fit} is a product of normalization parameters for a given run (i.e., for data taken at a given choice of angle and energy). There are 31 normalization parameters in the complete data set.

In our default fits, we enforce bounds on the form factor parameters by a χ^2 penalty,

$$\chi^2_b = \sum_{i=1}^{k_{max}} \left(\frac{a^2_{i,\text{fit}}}{|a_k|^2_{max}} + \frac{b^2_{i,\text{fit}}}{|b_k|^2_{max}} \right), \qquad (33)$$

where $a_{i,\text{fit}}$ and $b_{i,\text{fit}}$ are the fit values of the coefficients for G^p_E and G^p_M, respectively, and $|a_k|_{max}$ and $|b_k|_{max}$ are (Gaussian) bounds on the coefficients. For the polynomial and unbounded z expansion fits, $|a_k|_{max}$ and $|b_k|_{max}$ are taken to be very large, acting simply as numerical regulators in the fits (they are taken large enough such that fit results represent the infinite bound limit). For the bounded z expansion, Eq. (33) enforces a Gaussian, vs sharp cutoff, statistical prior on the form factor parameter space,[12] typically taken to be $|a_k/a_0|_{max} = |b_k/b_0|_{max} = 5$. A more detailed discussion of the dependence of fit results on form factor priors is postponed to Sec. VII C.

A. Polynomial and inverse polynomial fits

The radius central values, minimum χ^2, and reduced χ^2 are displayed in Table II for fits with form factors represented as polynomials in q^2 of degree 10, or as inverse polynomials of degree 7. These results are very close, but not identical, to the corresponding results in Table IV and Fig. 20 of Ref. [9]. We have compared our results to the output from the example fitting code provided as part of the Supplemental Material for Ref. [9], finding

TABLE II. Results for fits using polynomials of degree 10 and inverse polynomials of degree 7 for the full ($N_\sigma = 1422$) A1 MAMI data set. The reduced χ^2 is calculated taking $N_{dof} = N_\sigma - 2k_{max} - N_{norm}$ with $N_{norm} = 31$.

Fit type	r_E (fm)	r_M (fm)	χ^2	χ^2_{red}
poly 10	0.886	0.794	1561.6	1.14
inv poly 7	0.886	0.768	1569.1	1.14

agreement with the results of this code. For example, in the case of the polynomial of degree 10, the results of the example fitting code agree with our results in Table II, both having a minimum χ^2 of 1561.6, lower than the value 1563 quoted in Table IV of Ref. [9].[13]

B. Bounded z expansion fits

Let us proceed to consider the implications of the bounded z expansion. Here, we retain the identical data set as employed in Table II. For the default fit, we take $t_0 = 0$, $k_{max} = 12$, and a Gaussian bound of $|a_k|_{max} = |b_k|_{max}/\mu_p = 5$. The value $k_{max} = 12$ is large enough that the result does not change if k_{max} is increased further.

The results for this fit are displayed in Fig. 1 as a function of Q^2_{max}. The extracted radii and χ^2 values are provided for three Q^2_{max} values in Table III. The quoted uncertainty includes only the statistical-type uncertainties, i.e., counting statistics and uncorrelated systematic uncertainties that are represented by the rescaling of the statistical errors in the A1 data set. The uncertainty is obtained by varying the radius around the best-fit value, refitting the data while allowing all data set normalizations to float, to map out the χ^2 contour as a function of radius. The contours are typically symmetric and very nearly parabolic, and in the tables, we quote the average of the change in radius that yields $\Delta\chi^2 = 1$ on the high and low sides of the central value. Note that the primary A1 analysis of the Mainz data, identical except for the choice of the fitting function, yielded [9] $r_E = 0.879(5)_{stat}$ fm and $r_M = 0.777(13)_{stat}$ fm, including only statistical uncertainties for comparison with our bounded z expansion results in Table III.

C. Discussion

Let us remark on three aspects of the fits summarized in Table III. First, we remark that the bounded z expansion fit to the entire 1422 point data set ($Q^2_{max} = 1$ GeV^2) yields an electric radius significantly larger than the Mainz A1

---

[12]For a related discussion, see Ref. [69]. See also Ref. [70].

[13]More precisely, the fitting code returned a χ^2 of 1561.60 and $r_M = 0.797$ fm. Evaluating our χ^2 function with the corresponding parameters yielded an identical 1561.60. Using the same initialization conditions as the example fitting code, our minimization code independently returned a minimum χ^2 of 1561.58 and $r_M = 0.794$ fm, as displayed in Table II.

FIG. 1. Extracted electric (top panel) and magnetic (bottom panel) radii as functions of the kinematic cut Q^2_{max} on momentum transfer for the 1422 point A1 MAMI data set, using the z expansion with $t_0 = 0$, Gaussian priors with $|a_k|_{max} = |b_k|_{max}/\mu_p = 5$, $k_{max} = 12$. One-σ error bands are statistical only.

TABLE III. Results from the fits in Fig. 1 for three values of Q^2_{max}. N_σ is the number of cross section points with Q^2 below Q^2_{max}, and N_{norm} is the number of normalization parameters appearing in the data subset.

Q^2_{max} (GeV^2)	r_E (fm)	r_M (fm)	χ^2_{min}	N_σ	N_{norm}
0.05	0.873(18)	1.071(114)	479.4	483	13
0.5	0.905(10)	0.749(28)	1404.7	1285	29
1	0.920(9)	0.743(25)	1605.5	1422	31

$r_E = 0.920(9)_{stat}(6)_{other}$ fm, where for the moment we simply take the A1 evaluation of other contributions to the uncertainty.[14] This result is 7σ above the muonic hydrogen value, $r_E = 0.84087(30)$ fm [4]. It is also in tension with the results extracted from hydrogen spectroscopy, $r_E = 0.8758(77)$ fm [1], and with a previous global analysis [13] of world electron-proton scattering data which yielded $r_E = 0.875(10)$. The magnetic radius value of $r_M = 0.743(25)_{stat}(10)_{other}$ is almost 4σ from the value $r_M = 0.867(20)$ fm from the global analysis in Ref. [13]. However, we note that recent global analyses [13,14] use different representations of the form factors compared to the bounded z expansion used in Table III. In Sec. VII B below, we will perform our own analysis of the world data for a consistent comparison with the analysis of the Mainz data.

Simply replacing the fit functions employed in Ref. [9] with the z expansion does not resolve the discrepancy with muonic hydrogen results. In fact, the result is a larger difference with muonic hydrogen, as well as a tension with previous extractions from world electron-proton scattering data. In addition, the results show an unexpected dependence on the Q^2 range of data included in the fit. In the following Sec. VI, we consider in detail a range of sources of the systematic error before presenting best values for the radii.

D. Further tests related to the z expansion

1. Dependence on k_{max}

In the bounded z expansion, we may estimate the maximum power of z which can impact the data at a given level when the expansion coefficients a_n are order unity. Setting the upper limit of the contribution at the level of $\sim 0.5\%$ implies $k_{max} \approx 10$ should be sufficient for $t_0 = 0$, $Q^2_{max} = 1$ GeV^2. Figure 2 shows the χ^2 values and radii extracted as a function of k_{max} for the bounded z expansion fit to the full Mainz data set. The rightmost points at $k_{max} = 12$ correspond to the rightmost points in Fig. 1 and

extraction [9]. Having analyzed identical data sets, this difference arises solely from requiring the form factors to lie within the class allowed by the bounded z expansion. The difference, 0.041 fm, is large compared to the Mainz estimated systematic uncertainty. The magnetic radii exhibit a smaller difference, with our result 0.034 fm below the Mainz extracted value.

Second, the extracted radii have significant dependence on Q^2_{max}. For example, $r_E = 0.873(18)_{stat}$ fm with $Q^2_{max} = 0.05$ GeV^2 vs $r_E = 0.920(9)_{stat}$ fm with $Q^2_{max} = 1$ GeV^2. The difference, 0.047 fm, is again large compared to the quoted uncertainties. Furthermore, there is a non-negligible variation of the r_E central value as Q^2_{max} is increased above 0.5 GeV^2, even though the region below 0.5 GeV^2 includes more than 90% of the data points, and (as illustrated below in Fig. 10) the data above 0.5 GeV^2 do not significantly impact the radius uncertainty. In fits with unbounded parameters, it is not surprising that the extracted radius is sensitive to higher-Q^2 data because the radius may change to provide a better fit to fluctuations in the data that are accommodated by arbitrarily large parameter values. This behavior is unexpected in fits with bounded parameters. Thus, it is surprising that the small amount of higher-Q^2 data has such a significant impact on the extracted radius. The dependence on Q^2_{max} suggests a possible tension between the lower- and higher-Q^2 data.

Third, taking at face value the complete 1422 point data set and error assignments, the resulting electric radius is

---

[14]The error $(6)_{other}$ results from the quadrature sum for the errors $(4)_{syst}(2)_{model}(4)_{group}$ presented in Ref. [9]. These errors were added in quadrature in Ref. [9], but it has more recently been advocated [10] to add the final error linearly to the quadrature sum of the first two, resulting in $\sim(8.5)_{other}$.
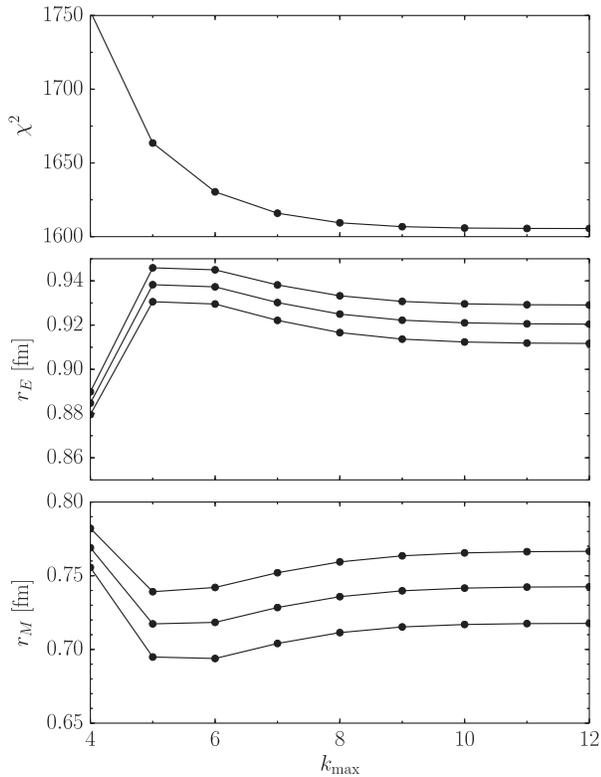
FIG. 2. Total χ^2 (top panel) and extracted electric (middle panel) and magnetic (bottom panel) radii as functions of $k_{\max}$ for the 1422 point A1 MAMI data set, using the z expansion with $t_0 = 0$, Gaussian priors with $|a_k|_{\max} = |b_k|_{\max}/\mu_p = 5$. One-$\sigma$ error bands are statistical only.

FIG. 3 (color online). χ^2 (top panel, solid black line) and extracted electric (middle panel, solid black lines) and magnetic (bottom panel, solid black lines) radii with 1σ statistical error bands as functions of $k_{\max}$ for the unbounded z expansion fit with $t_0 = 0$ to the 1422 point A1 MAMI data set (with floating normalization). The dashed blue lines show the χ^2 and 1σ error bands from the bounded fit in Fig. 2 for comparison.

to the final row of Table III. In accordance with our power counting estimate, the minimum χ^2 value and extracted radii have stabilized by $k_{\max} = 10$. For definiteness, we choose $k_{\max} = 12$ for all of our bounded z expansion fits. While this is significantly more parameters than required for fits to smaller values of $Q^2_{\max}$, the bounds on the fit parameters prevent the problem of radius instability due to overfitting of noise in the higher-Q^2 data [11].

2. Unbounded z expansion fits

The bounded z expansion (the formal $k_{\max} \to \infty$ limit with bounded coefficients) is a particularly well-motivated implementation of form factor priors. A different but common choice of priors corresponds to setting $a_k = 0$ for all coefficients beyond a given order $k > k_{\max}$, with the remaining coefficients unconstrained, and $-\infty < a_k < \infty$ for $k \leq k_{\max}$. We perform some illustrative fits with this modified choice of priors in order to separate the impact of applying bounds from the impact of changing from polynomial or inverse polynomial functions to the z expansion. We again fit the 1422 point A1 data set using the same rescaled errors and Feshbach TPE correction as in Fig. 1, but now set $|a_k|_{\max}, |b_k|_{\max} \to \infty$ in Eq. (33).

In the limit of large $k_{\max}$, the true form factors are guaranteed to lie in the space of curves described by the unbounded z expansion. However, many badly behaved form factors (in particular, form factors in conflict with predictions of QCD, as discussed in Sec. III) also lie in this space of curves, and fits without constraints on the coefficients lose predictive power at large $k_{\max}$.

Figure 3 shows results for unbounded fits with floating normalizations. The minimum χ^2 value continues to decrease significantly as parameters are added through $k_{\max} = 10$. Quantitatively reliable radius estimates are difficult to obtain from such a fit; for small $k_{\max}$, omitted terms in the form factor expansion can introduce a potentially large, but difficult to quantify, bias in the fitted radii [71], while for large $k_{\max}$, the uncertainties grow rapidly.

3. Fixed-normalization fits

As noted earlier, the manner in which uncorrelated systematic uncertainties are treated in the Mainz data set is only complete when the normalization parameters are allowed to vary and when correlated systematic uncertainties are estimated separately [9]. Thus, fits which fix the
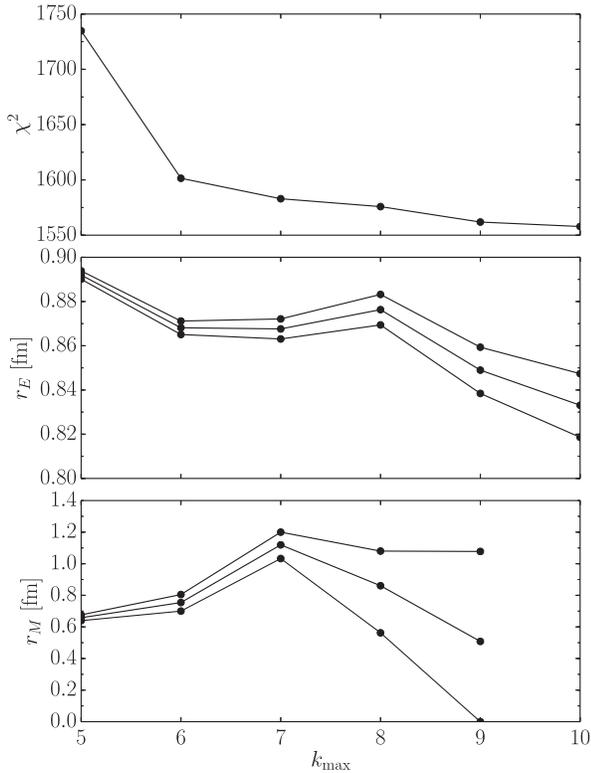
FIG. 4. χ^2 (top panel) and extracted electric (middle panel) and magnetic (bottom panel) radii with 1σ statistical error bands as functions of k_{max} for the unbounded z expansion fit with $t_0 = 0$ to the 1422 point A1 MAMI data set with fixed normalization parameters.

normalization of the data based on the default Mainz fit will underestimate uncertainties and potentially yield different values for the radii if the fit is performed with a different functional form than that used to determine the normalization parameters. Nonetheless, such fits have been performed [8,72], and so we provide a comparison of unbounded fits with and without floating normalization factors.

The result for fixed normalization factors is displayed in Fig. 4. Comparing to fits with floating normalizations, one can see that the uncertainties are significantly smaller in the case of fixed normalizations, with the fit uncertainties on r_E underestimated by a factor $\gtrsim 5$.[15]

Even ignoring the artificially small uncertainties that arise when neglecting the normalization uncertainty of the data sets, it is not clear that there is any value of k_{max} for which the fit provides a sufficiently precise description of the data while still providing meaningful uncertainties on the charge radius. For the magnetic radius, the results are even less clear, with only an upper limit on the radius

possible for $k_{max} \geq 9$. We note that for large k_{max} the r_E central values for the fits displayed in Figs. 3 and 4 require very large coefficient values, in violent conflict with order unity predictions of QCD.[16]

VI. SYSTEMATIC STUDIES FOR THE MAINZ DATA SET

Taking the data and error prescriptions of Ref. [9] at face value, we have found radius extractions in tension with each other for fits of different functions to the same data set (Table II compared to the last line of Table III) and for fits of the same function to subsets of the same data set (Fig. 1 and Table III).

The first observation indicates the strong dependence of the extracted radius on the specification of physical form factors, as implemented by the bounded z expansion. We focus solely on this class of form factors in the following. Since the systematic error analysis of Ref. [9] relied on rescaling statistical errors based on fits to a particular class of form factor models, we also revisit this analysis using the bounded z expansion.

The second observation, that fits to data subsets are in tension with fits to the entire data set, indicates the possibility of an underestimated systematic error. We investigate below a range of correlated errors and their potential impact on radius extractions.

The analysis of the Mainz data by the A1 Collaboration decomposed the uncertainties into several different contributions. Let us briefly review this decomposition. The only uncertainty applied directly to the quoted cross sections is called the statistical uncertainty. This is a combination of counting statistics and systematic uncertainties which are taken to be uncorrelated between different data points and normally distributed and is thus treated in the same way as counting statistics. We refer to the systematic uncertainties that are independent for different data points as the uncorrelated systematic uncertainties. The A1 Collaboration includes these uncorrelated systematic uncertainties by introducing a rescaling factor on the counting statistics, with a procedure to extract these scaling factors which we summarize below in Sec. VI B 1.

Normalization uncertainties for each data subset in the experiment are accounted for in the extraction of the radius by allowing the 31 normalization factors corresponding to different configurations to float freely when fitting the form factors. The A1 analysis of Ref. [9] suggests an uncertainty of 3.5%–5% on the normalization factors, but no constraints were included in the fits. Because the cross sections are quoted after the determination of the normalization factors in their fit, any information on the initial normalizations is lost, and it is no longer possible for us to make

---

[15]In detail, for $k_{max} = 9(10)$, the radius uncertainty is $\delta r_E = 0.011(0.014)$ for fixed normalizations, compared to $\delta r_E = 0.053(0.096)$ for floating normalizations.

[16]For example, at $k_{max} = 9$, requiring the central value for r_E in Fig. 4 to lie within the 1σ envelope of a bounded z expansion requires coefficient bound $\gtrsim 10^4$.

use of even the limited precision with which these normalization factors were constrained.

Finally, the A1 Collaboration gives a procedure for estimating the impact of correlated systematic uncertainties on their data. These are corrections which potentially have a strong kinematic dependence, and their impact will not necessarily decrease when one includes a large number of measurements. Such corrections must be treated independently from the statistical and uncorrelated systematic errors. The Mainz treatment of these uncertainties and our examination of other possible correlated effects are included in Sec. VI C.

In the remainder of this section, we introduce the following three modifications to the analysis. First, in Sec. VI A, we study the impact of different TPE correction models on radius extractions, choosing the SIFF sum of monopoles ansatz as the default in the remaining fits. Second, after identifying in Sec. VI B 1 potential shortcomings in the rescaling of statistical errors, in Sec. VI B 2, we rebin data taken at identical kinematic settings in order to incorporate in Sec. VI B 3 uncorrelated systematic errors which do not scale with statistics. Lastly, in Sec. VI C, we consider a range of correlated systematic errors consistent with the experimental precision achieved in Ref. [9].

A. TPE model dependence

The variation of the extracted radii with different TPE models is illustrated in Fig. 5, where the extracted r_E and r_M central values are plotted vs Q^2_{max}. The black curve is identical to the central curve in Fig. 1. The remaining results are obtained by repeating the fit of Sec. V after removing the Feshbach TPE correction, Eq. (27), and then applying the SIFF TPE result [using dipole form factors, Eq. (24), or those from Blunden *et al.*, Eq. (25)] or applying no finite TPE correction [in the Maximon–Tjon convention, Eq. (26)]. As the plot illustrates, expressed as a difference relative to the Feshbach correction, the results have mild Q^2_{max} dependence. Numerical values for $Q^2_{max} = 0.05, 0.5, 1$ GeV^2 are given in Table IV.

The Feshbach correction is the exact result in the formal limit of infinite proton mass and is independent of the proton structure. The exact result for arbitrary kinematics for a pointlike proton [38] yields a correction that grows with Q^2, approximately doubling the correction between $Q^2 = 0$ and 1 GeV^2. However, calculations using either hadronic [35] or partonic [37] models to account for proton structure indicate that the correction does not grow with increasing Q^2 but instead becomes smaller and then changes sign. This is the behavior required to explain the difference between the Rosenbluth and polarization measurements of $\mu_p G_E / G_M$ for the proton [24] and has been recently confirmed for $Q^2 \approx 1$–1.5 GeV^2 by comparisons of positron and electron scattering from the proton [73,74].
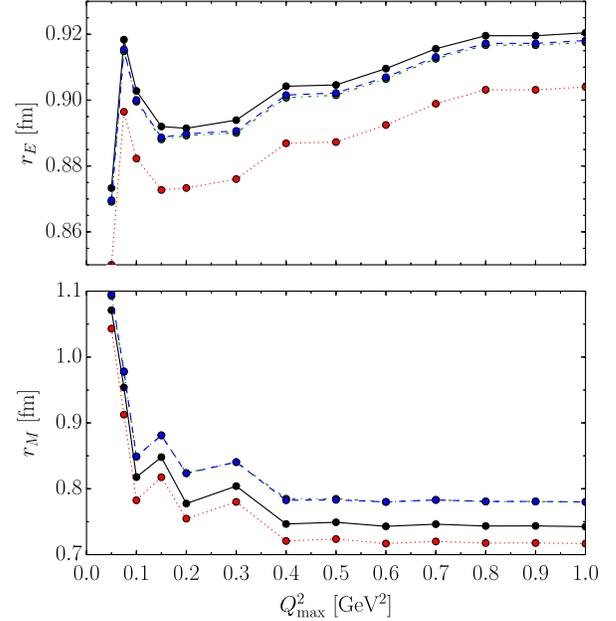
FIG. 5 (color online). Extracted electric (top panel) and magnetic (bottom panel) radii as functions of the kinematic cut Q^2_{max} on momentum transfer for several TPE models, as discussed in the text: no correction (red, dotted), Feshbach correction (black, solid), SIFF dipole (green, dot-dashed), and SIFF sum of monopoles (blue, dashed). There is a negligible difference between the SIFF choices of the dipole and the sum of monopoles. Fits are to the 1422 point A1 MAMI data set, using the z expansion with $t_0 = 0$, Gaussian priors with $|a_k|_{max} = |b_k|_{max}/\mu_p = 5$, $k_{max} = 12$.

There is a significant difference in the charge radius between the case of no TPE corrections and either the Feshbach or SIFF corrections. However, there is a relatively small difference between Feshbach and SIFF, suggesting that the infinite proton mass limit provides a significant part

TABLE IV. Change in the extracted charge and magnetic radii for three different TPE corrections, relative to the Feshbach correction applied in the Mainz analysis. Results are for the fit with $Q^2_{max} = 0.05, 0.5, 1$ GeV^2 in Fig. 5.

Q^2_{max} (GeV^2)	Model	Δr_E (fm)	Δr_M (fm)
0.05	Feshbach	$\equiv 0$	$\equiv 0$
	SIFF dipole	-0.004	$+0.022$
	SIFF Blunden	-0.004	$+0.025$
	No TPE	-0.023	-0.028
0.5	Feshbach	$\equiv 0$	$\equiv 0$
	SIFF dipole	-0.003	$+0.036$
	SIFF Blunden	-0.002	$+0.034$
	No TPE	-0.017	-0.026
1	Feshbach	$\equiv 0$	$\equiv 0$
	SIFF dipole	-0.003	$+0.038$
	SIFF Blunden	-0.002	$+0.037$
	No TPE	-0.016	-0.026

of the correction for r_E. For the magnetic radius, there is a large difference between all three approaches. For both the charge and magnetic radii, there is little sensitivity to the choice of form factors included in the SIFF calculation. We collect in Table IV the deviations of the extracted radius using different models in place of the Feshbach correction. In all subsequent fits, we employ the SIFF ansatz, using for definiteness the sum of monopoles in Table I as our default TPE model. The uncertainty associated with TPE corrections will be incorporated into the evaluation of correlated systematic uncertainties in Sec. VI C.

B. Uncorrelated systematic uncertainties

1. Summary of the Mainz A1 approach

To estimate the uncorrelated systematic uncertainties, the A1 Collaboration performed a fit to the entire 1422 point data set using a default form factor model (an eight-parameter cubic spline model for each of G_E and G_M). The data were then grouped according to the beam energy and the spectrometer used in the measurement. For each data group, the uncorrelated systematic uncertainties were taken from examination of the distribution of the differences between measured and fit cross sections, scaled by the uncertainty from counting statistics. (If the counting statistics fully represented the uncorrelated uncertainties, then this should be a Gaussian distribution with width one.) This distribution was fit with a Gaussian, the width of which was then taken as the scaling factor applied to the counting statistics to determine the combined statistical and systematic uncorrelated uncertainties. The scaling factors obtained in this way vary from 1.070 to 2.283, as given in the Supplemental Material of Ref. [9].

This rescaling procedure is meant to yield a reduced χ^2 close to unity when the data are compared to the original fit. However, because the Gaussian fit may underestimate the impact of outliers and the scaling of the uncertainties changes the relative weighting of the different data sets, the fit to the data set with updated uncertainties yields a reduced χ^2 somewhat larger than unity: $\chi^2_{red} \approx 1.15$ for the entire data set. This suggests that the quoted systematics are somewhat underestimated.

The rescaled statistical errors represent the minimum additional uncertainty necessary to account for random scatter around a global fit to the data. Any correlated effects will not be included in the extracted uncertainties. For example, the A1 analysis of Ref. [9] does not include any uncertainty associated with the error in the measurement of the beam energy or offsets in the spectrometer angles. Such kinematic offsets would yield correlated errors in the cross sections which would not be captured by this procedure.

The A1 rescaling procedure yields systematic uncertainties which depend on the form factor model used in the fit. We performed a similar analysis using our bounded z expansion and using the χ^2 value for each data subset

relative to the fit as the square of the scaling factor. This procedure yielded similar scaling factors, larger by 6% on average compared to the A1 procedure (thus yielding a value of χ^2_{red} closer to unity), with a typical scatter around the small average offset of approximately 10%. Thus, the form factor model dependence of this rescaling procedure is small, though not negligible, and related more to the difference in our procedure than to the change in the fitting function.

The rescaling procedure accounts for undetermined systematic errors that are assumed to be uncorrelated and to scale with the statistical counting errors. However, it is not clear that all the uncorrelated systematics should scale with the statistical uncertainties. If one assumes that the statistical and uncorrelated systematic uncertainties add in quadrature, then one can compare the original (unscaled) and rescaled statistical uncertainties to extract the effective uncorrelated systematic uncertainty used in the A1 procedure. This inferred uncertainty can be extremely small, as low as 0.05%, but varies with kinematics and with the counting statistics, attaining values up to 2%. Because the full set of 1422 data points includes many instances of repeated measurements at identical kinematics, this procedure implies even greater reduction in the systematic uncertainty associated with each independent kinematic point, with values as low as 0.02%, even though it is experimentally difficult to constrain uncertainties at that level.

To address these concerns, we present a modified treatment of the uncorrelated systematic uncertainties where a fixed uncorrelated systematic error is added to all points to account for unknown drifts or corrections.

2. Rebinning studies

As noted above, the 1422 data points include many repeated measurements at the same conditions. One would expect that many potential systematic errors would be identical for these points, e.g., time-dependent efficiencies, rate-dependent corrections, or uncertainties in the beam energy or spectrometer angle settings. Adding a fixed systematic to every one of the 1422 data points would underestimate the systematic uncertainty for data points with many repeated measurements. Therefore, we begin by combining data points taken with identical conditions, reducing the data set from 1422 data points to 658 independent cross section measurements.

We group (i.e., rebin) all data taken at identical kinematic settings, using only the uncertainties from counting statistics (i.e. removing the A1 scaling factor). We tested our assumption that the points within the groups of repeated measurements were consistent within statistics by looking at the χ^2 values and confidence levels for every set of the rebinned data. There were 407 settings with multiple runs taken under identical conditions, and the confidence-level distribution for these sets is consistent with a uniform

distribution between 0% and 100% except for a handful of outliers below 1% confidence level, indicating a nonstatistical scatter of the points being combined. Most of these outliers involved scatter at the 0.1%–0.2% level, which is contained within the systematic uncertainty we will add to achieve $\chi^2_{\rm red}$ near unity. One setting—$E_{\rm beam} = 315$ MeV, $\theta = 30.01°$, spectrometer C—had a single measurement that deviated by ~1.5% from the two other measurements at that setting, while the statistical uncertainties were approximately 0.15%. We excluded this set of points, yielding a total of 657 independent cross section measurements when fitting the rebinned data.

We remark that normalization parameter 14 appears for only one point in the rebinned 657 point data set (and two points in the original 1422 point data set). Since the normalization parameters have to be allowed to float freely in the fit, this data point has no impact, but for definiteness, it is retained. Note that with the Mainz procedure of applying scaling factors to the counting statistics the rebinning has no impact on the fit, and the only change at this point would be due to the exclusion of the one point after rebinning. However, when applying a more conventional constant uncorrelated systematic uncertainty to all points, the uncertainty is best applied to the rebinned data points.

3. Uncorrelated systematics for rebinned data

With the rebinned data set in hand, we proceed to investigate the inclusion of an uncorrelated systematic error that does not scale with statistics. We add a fixed systematic uncertainty to every data point and perform the bounded z expansion fit with $Q^2_{\rm max} = 1$ GeV^2 and our default form factor scheme, $t_0 = 0$, $k_{\rm max} = 12$, and Gaussian bound $|a_k|_{\rm max} = |b_k|_{\rm max}/\mu_p = 5$. We varied the systematic uncertainty until we found a reduced χ^2 value close to unity. This required a systematic uncertainty of approximately 0.3%. We then examined the χ^2 contribution from each of the 18 energy-spectrometer combinations to see if any of them had anomalously large or small $\chi^2_{\rm red}$ values. While the spread of $\chi^2_{\rm red}$ values was significant, many data subsets had a relatively small number of points, and the only subset which was an extreme outlier was the data from spectrometer B at $E_{\rm beam} = 855$ MeV. We chose to increase the systematic uncertainty on this data subset to 0.4% while keeping 0.3% for all other data subsets. The reduced χ^2 and confidence levels for each data subset are displayed in Table V. The total χ^2 is 520.4 for 657 points, which might suggest that 0.3% is a slight overestimate of the uncorrelated systematic, but it is a small effect, with a 0.25% correction yielding a reduced χ^2 above 1 by a similar amount.

Table VI shows the radius fit results for the rebinned Mainz data with the statistical scaling factors from the original analysis replaced by the constant 0.3% systematic uncertainty (0.4% for spectrometer B at 855 MeV beam energy).

TABLE V. Number of data points, reduced χ^2, and confidence level for each combination of spectrometer (A, B, or C) and beam energy (in MeV) of the rebinned A1 MAMI data set. Columns 4 and 5 give the results after the inclusion of a uniform 0.25% uncorrelated systematic; columns 6 and 7 give the results after the inclusion of the final 0.3–0.4% uncorrelated systematic. See the text for details.

Spec.	Beam	N_σ	$\chi^2_{\rm red}$	C.L. (%)	$\chi^2_{\rm red}$	C.L. (%)
A	180	29	0.59	96.1	0.46	99.4
	315	23	0.54	96.4	0.44	99.1
	450	25	1.52	4.8	1.00	46.7
	585	28	1.54	3.4	1.03	42.8
	720	29	1.05	39.9	0.87	66.4
	855	21	0.92	56.8	0.77	76.0
B	180	61	0.85	79.8	0.65	98.3
	315	46	1.05	38.5	0.76	88.5
	450	68	0.90	71.7	0.67	98.2
	585	60	0.61	99.2	0.50	99.96
	720	57	1.29	6.9	0.97	53.7
	855	66	1.88	0.002	1.15	19.6
C	180	24	0.88	63.3	0.68	88.0
	315	24	1.16	27.2	0.78	76.8
	450	25	1.53	4.3	1.08	35.9
	585	18	0.83	66.3	0.65	86.4
	720	32	1.11	30.2	0.90	62.3
	855	21	0.79	73.7	0.62	90.5

This procedure introduces enough uncertainty to account for random scatter of the points around the best-fit curve. However, any errors that are correlated between multiple points will bias the fit, and will not be fully reflected in this procedure, making the resulting uncertainty estimate more of a lower limit. While the impact of correlated uncertainties will be examined separately, these rely on specific models for kinematic dependences of any additional errors. The inclusion of an even larger uncorrelated uncertainty would allow the data to account for a range of correlated errors, but the reduced χ^2 would end up significantly smaller than unity. For illustration, Table VII shows the results where we apply a 0.5% uncorrelated systematic uncertainty to every data point, instead of the 0.3%–0.4% uncertainties in the previous fit.

TABLE VI. Results for fitting of the 657 point rebinned A1 MAMI data set with 0.3%–0.4% uncorrelated systematic uncertainties at three values of $Q^2_{\rm max}$ using the z expansion with $t_0 = 0$, Gaussian priors with $|a_k|_{\rm max} = |b_k|_{\rm max}/\mu_p = 5$, $k_{\rm max} = 12$. N_σ is the number of cross section points with $Q^2 < Q^2_{\rm max}$, and $N_{\rm norm}$ is the number of normalization parameters appearing in the data subset.

$Q^2_{\rm max}$ (GeV^2)	r_E (fm)	r_M (fm)	$\chi^2_{\rm min}$	N_σ	$N_{\rm norm}$
0.05	0.856(27)	1.11(14)	110.5	176	13
0.5	0.895(14)	0.777(34)	442.0	568	29
1	0.908(13)	0.767(33)	520.4	657	31

TABLE VII. Same as Table VI, but with 0.5% uncorrelated systematic uncertainty.

$Q^2_{\max}$ (GeV^2)	r_E (fm)	r_M (fm)	$\chi^2_{\min}$	N_σ	N_{norm}
0.05	0.861(35)	1.05(18)	48.7	176	13
0.5	0.891(18)	0.768(43)	211.5	568	29
1	0.901(17)	0.758(42)	250.3	657	31

C. Correlated systematic uncertainties

We now consider systematic errors that do not scale with statistical errors but that are also correlated across data points. We begin by examining the procedure of Ref. [9]. We then examine modified evaluations of the radius uncertainty associated with the correlated systematic uncertainties.

1. Summary of the Mainz A1 approach

In the A1 MAMI data set, each cross section is accompanied by two factors to account for systematic uncertainties. The first is due to the bremsstrahlung energy cut and is estimated by varying the cut. The second is meant to account for efficiency changes, normalization drifts, variations in spectrometer acceptance, and background misestimations. This second class of systematics is investigated by applying a kinematic-dependent correction to the data. The complete data set is refit after multiplying or dividing the individual cross section ratios by the corresponding factor for either the energy cut or correlated systematic error, and the largest difference in radius obtained from multiplying or dividing is taken as the uncertainty. The total systematic uncertainty is then obtained by summing in quadrature:

$$\Delta r_{\mathrm{syst}} = \sqrt{(\Delta r_{\mathrm{Ecut}})^2 + (\Delta r_{\mathrm{corr}})^2}. \tag{34}$$

The stated cross section uncertainties associated with the variation in the energy cut are small, with a rms variation of 0.08%. These mainly introduce an additional scatter into the cross sections but have little impact on the radius central values. For the entire data set, this translates to an uncertainty in r_E of 0.003 fm and in r_M of 0.009 fm. Explicit results are given in Table VIII.

In the A1 analysis, the kinematic-dependent correlated systematic is assumed to depend linearly on the scattering angle [cf. Eq. (35) below, with $x = \theta$], with a variation of approximately 0.2% between the minimum and maximum angles for each energy-spectrometer combination, except the 855 MeV data with spectrometer C (covering large angles), for which the variation is approximately 0.5%.[17]

---

[17]These values are deduced from the appropriate column of the tabulated data set in the Supplemental Material of Ref. [9].

TABLE VIII. Results for changes in the radii under increases (upper value for each $Q^2_{\max}$) or decreases (lower value) in the energy loss cut. Fits are for the 657 point rebinned A1 MAMI data set with 0.3%–0.4% uncorrelated systematic uncertainties at three values of $Q^2_{\max}$ using the z expansion with $t_0 = 0$, Gaussian priors with $|a_k|_{\max} = |b_k|_{\max}/\mu_p = 5$, $k_{\max} = 12$.

$Q^2_{\max}$ (GeV^2)	Δr_E (fm)	Δr_M (fm)
0.05	−0.001	+0.023
	−0.005	0.000
0.5	+0.003	+0.003
	−0.003	+0.003
1	+0.003	+0.009
	−0.002	0.000

We perform a more comprehensive study of correlated systematics below.

2. Sensitivity to size or kinematic dependence

The correlated systematics mentioned above could represent either experimental or theoretical uncertainties. For example, they could be associated with radiative corrections (beyond the energy cutoff variation), background subtraction [14], potential offsets in the absolute beam energy or angle calibration, etc. The impact of such uncertainties on the cross sections is difficult to constrain below the 0.5% level, but because of the floating normalizations of the different data sets, these correlated systematic uncertainties only need to account for the variation within a specific normalization subset.

While some sources of correlated corrections may be well approximated by a correction that is linear in the scattering angle over a single energy-spectrometer setting, this is not the only possible kinematic dependence, and effects may be relevant over larger or smaller subsets of data or may be more important for one spectrometer. Thus, we examine the impact of different prescriptions for applying the correlated systematics. We take a 0.5% variation in the systematic correction but vary the functional form used to go from the minimum to the maximum kinematic settings within data subsets, and we vary how the full experiment is broken down. For the latter, we examine three cases: 0.5% variation over the range of angles for each spectrometer-energy combination (as done in the A1 analysis, with 18 separate angular ranges), 0.5% variation over the full kinematic range for each spectrometer (with three separate ranges), and 0.5% variation for each of the 34 normalization subsets.

We examine eight different approaches to varying the kinematic dependence of the systematic correction over a given data subset. We multiply and divide the cross sections and uncertainties by the factor

$$1 + \delta_{\mathrm{corr}} = 1 + a \frac{x - x_{\min}}{x_{\max} - x_{\min}}, \tag{35}$$

where $a = 0.005$ and x is a kinematic variable. We take the variable x to be proportional or inversely proportional to θ, Q^2, or E' or to be proportional to ε or $1/\sin^4(\theta/2)$. Note that for a given energy the correction goes from zero at one extreme of the angular range for the data subset to 0.5% at the other extreme; these different corrections only modify the interpolation to intermediate angles. These illustrative functional forms can be motivated from specific sources, including kinematic offsets, rate-dependent effects, or simplified models of radiative corrections. However, the exact magnitude and precise functional form cannot be fully determined without further input.

Taking the correction to be linear in the scattering angle, $x = \theta$, and applied to each of the 18 energy-spectrometer combinations, we find an uncertainty in the radii from fits to the entire data set of $\Delta r_E = 0.017$ fm, $\Delta r_M = 0.025$ fm. These are roughly 2.5 times larger than the values quoted in the Mainz analysis, due mainly to the increase from their $\sim 0.2\%$ to our 0.5%. Other functional forms give similar results, with the largest effect coming from scaling the uncertainties with $1/Q^2$. The cases $x = Q^2$, $1/Q^2$, θ, and $1/\theta$ are given in Table IX. We take the case $x = \theta$ to represent a reasonable average of the functional forms tested.

3. Impact of applying systematic corrections to different data subsets

Applying the 0.5% correction over the full kinematic range for each spectrometer, rather than over the range corresponding to a single beam energy, yielded somewhat smaller uncertainties for r_E and somewhat larger uncertainties for r_M. There was also a wider spread in the

TABLE IX. Results for changes in the radii under multiplication (top sign) or division (bottom sign) by a linear perturbation as in Eq. (35) for each beam energy/spectrometer combination, with $x = Q^2$, $1/Q^2$, θ, or $1/\theta$. Fits are for the 657 point rebinned A1 MAMI data set with 0.3%–0.4% uncorrelated systematic uncertainties at three values of $Q^2_{\max}$ using the z expansion with $t_0 = 0$, Gaussian priors with $|a_k|_{\max} = |b_k|_{\max}/\mu_p = 5$, $k_{\max} = 12$.

x	$Q^2_{\max}$ (GeV^2)	Δr_E (fm)	Δr_M (fm)
Q^2	0.05	∓ 0.017	± 0.021
	0.5	∓ 0.016	∓ 0.022
	1	∓ 0.015	∓ 0.026
$1/Q^2$	0.05	± 0.041	∓ 0.046
	0.5	± 0.025	± 0.016
	1	± 0.023	± 0.021
θ	0.05	∓ 0.022	± 0.027
	0.5	∓ 0.018	∓ 0.021
	1	∓ 0.017	∓ 0.025
$1/\theta$	0.05	± 0.036	∓ 0.039
	0.5	± 0.024	± 0.018
	1	± 0.021	± 0.022

uncertainties arising from different functional forms in Eq. (35), as expected for the interpolation over a wider kinematic range. Applying the 0.5% variation only over the angular range for each normalization subset yielded uncertainties that were typically 20%–30% larger for r_E compared to the default approach, with smaller increases for the uncertainty on r_M. We note that similar studies using the original 1422 point data set showed much larger increases when applying the correction to the different normalization subsets.

For simplicity, we have taken the systematic scaling factor, a in Eq. (35), identical in sign (i.e., always multiplying or always dividing by $1 + \delta_{\rm corr}$) and magnitude for each data subset. However, many systematic effects could differ for the different spectrometers, and the combined effect might be enhanced or suppressed by the assumption of identical corrections. When applied individually to each spectrometer, the charge radius uncertainty tends to be dominated by the corrections applied to spectrometer B. For the magnetic radius, there tends to be a significant cancellation between the corrections from the three spectrometers, and the result of shifting all of the spectrometers identically (used in Ref. [9] and shown in Table IX) is much smaller than the result of evaluating the corrections independently for each spectrometer. Because it is not clear how much the spectrometer corrections may be related, we do not enhance the uncertainty in r_M. We simply note that the uncertainty on r_M shown in Table IX could be a significant underestimate if the cancellation in these tests does not reflect the true nature of any systematic corrections.

To further investigate the impact of applying different correlated systematic shifts to different data subsets, consider a fit with distinct parameters a in Eq. (35) for different data subsets. These are allowed to vary as part of the fit, which then allows for subpercent kinematic variations in each data subset. This could be done with separate parameters for each spectrometer, for each of the 18 energy-spectrometer combinations or for each of the 34 different normalization subsets. For definiteness, we consider a fit with an independent normalization and slope parameter a for each of the 34 normalization subsets.[18] This seems most consistent with the breakdown of uncertainties into normalization, correlated systematics, and uncorrelated systematics. For $Q^2_{\max} = 0.5$ GeV^2, we find $r_E = 0.891(18)$ fm and $r_M = 0.792(49)$ fm, compared to $r_E = 0.895(20)$ fm and $r_M = 0.776(38)$ fm from Table X below, which includes both statistical and uncorrelated systematic uncertainties. The changes in the extracted radii are consistent with the previously assigned uncertainties

---

[18]Note that in the Mainz analysis and our other fits there are 31 normalization parameters which appear in 34 different combinations. For this test, we allow all 34 normalization factors to vary independently.

TABLE X.   Final radius results from the fits to the rebinned 657 point A1 MAMI data set with the 0.3%–0.4% uncorrelated systematic uncertainties in Fig. 6, for three values of Q^2_{max}. The uncertainties labeled "stat" include both the statistical and uncorrelated systematic uncertainties, while those labeled "ΔE" and "cor" account for the energy cut dependence and the correlated systematic uncertainties, respectively.

Q^2_{max} (GeV^2)	r_E (fm)	r_M (fm)
0.05	$0.856(27)_{stat}(5)_{\Delta E}(18)_{cor}$	$1.11(14)_{stat}(2)_{\Delta E}(2)_{cor}$
0.5	$0.895(14)_{stat}(3)_{\Delta E}(14)_{cor}$	$0.776(34)_{stat}(3)_{\Delta E}(17)_{cor}$
1	$0.908(13)_{stat}(3)_{\Delta E}(14)_{cor}$	$0.766(33)_{stat}(9)_{\Delta E}(20)_{cor}$

associated with the correlated systematics. The uncertainties in this fit are somewhat smaller for the charge radius and larger for the magnetic radius, in line with the expectation based on applying the corrections separately to each spectrometer. This may be a more realistic estimate of the uncertainties and could potentially allow for a combined analysis of Mainz and world data by including all of the Mainz systematic uncertainties explicitly in the fit. However, most likely neither the Mainz assumption that the corrections are totally correlated between settings nor the assumption here that they are totally uncorrelated is entirely realistic. The analysis presented here is included only as an independent estimate of the impact of allowing the correlated systematic correction to differ for different kinematic settings.

4. Final evaluation of the correlated systematics

It is difficult to determine an optimal approach for evaluating the impact of unknown systematic errors or corrections. The analysis strategy for the Mainz data set involves a breakdown of the uncertainties into uncorrelated, correlated, and normalization contributions and seems most consistent with applying the correlated uncertainty to each normalization subset. As noted above, this tends to increase the uncertainty on r_E in comparison to applying the correlated uncertainty to each spectrometer or to each spectrometer-energy combination. Similarly, applying corrections independently to the three spectrometers tends to decrease the uncertainty on r_E and increase the uncertainty on r_M.

We choose to evaluate the correlated systematic error by making simple, minimal changes to the A1 procedure. We evaluate the impact of a linear angle-dependent correction ($x = \theta$), applied to each beam-spectrometer combination, but choose a fixed 0.4% variation. The 0.4% variation ($a = 0.004$) is approximately twice the typical value considered in the A1 analysis, which seems a reasonable estimate to account for additional systematic effects such as TPE [12] and background subtraction [14]. At $Q^2_{max} = 1$ GeV^2, this choice yields uncertainties of 0.014 fm and

0.020 fm for r_E and r_M, respectively, four-fifths of the uncertainties shown for $x = \theta$ in Table IX.

These uncertainties are significant, but not sufficient to explain the discrepancy with muonic hydrogen. Obtaining larger shifts due to such corrections would require either a systematic shift above the 0.4% assumed here, a correction applied over smaller data subsets, a more extreme functional form for such corrections than considered here, or a conspiracy between shifts applied to different spectrometer-beam combinations.

VII. RADIUS RESULTS FROM MAINZ AND WORLD DATA

Having completed our systematics studies, we proceed to perform a final fit to the Mainz data and compare with a fit to other world data using the same theoretical framework. We close this section with several consistency checks on the fits, including a discussion of form factor priors, radiative corrections beyond TPE, and the verification of the fit consistency between different spectrometer-energy subsets of the data.

A. Best fit radii from Mainz data

Let us summarize our final fit to the Mainz data set. We use the 657 point rebinned data set of Sec. VI B 2, with the SIFF sum of monopoles TPE correction from Table I in place of the Feshbach correction applied in the Mainz analysis and with the A1 statistical rescaling replaced by a fixed 0.3%–0.4% uncorrelated systematic as in Sec. VI B 3. We employ our default form factor scheme, $t_0 = 0$, $k_{max} = 12$, and Gaussian bound $|a_k|_{max} = |b_k|_{max}/\mu_p = 5$. The results are shown in Fig. 6 and Table X. The "statistical" uncertainty accounts for both counting statistics and the uncorrelated systematic uncertainties. The energy cut correction is taken from Table VIII. The correlated systematic uncertainty is obtained from the $x = \theta$ entry of Table IX, rescaled to 0.4%, as described above in Sec. VI C 4.

B. Best fit radii from world data

Now that we have a procedure for analyzing the Mainz data, we perform a similar fit to the global set of world data, excluding the Mainz data set. We perform this separate analysis in part to obtain independent results as a check on consistency between the Mainz data set and the world data set. In addition, it is not clear that there is a reliable way to perform a combined analysis of the Mainz data with other experiments, given the very different manner in which uncertainties from the Mainz experiment were presented [11]. The inclusion of the correlated systematic correction coefficients a in the fit, as discussed in Sec. VI C 3, yields a fit to the Mainz data where all uncertainties are accounted for in the fit and would allow a combined analysis with the
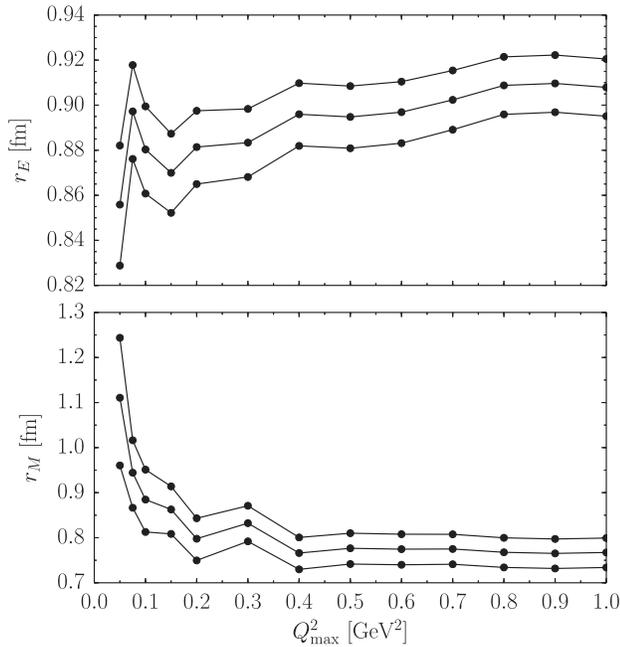
FIG. 6.   Extracted electric (top panel) and magnetic (bottom panel) radii as functions of the kinematic cut Q^2_{max} on the momentum transfer for the rebinned 657 point A1 MAMI data set, with 0.3%–0.4% uncorrelated systematic uncertainties, using the z expansion with $t_0 = 0$, Gaussian priors with $|a_k|_{max} = |b_k|_{max}/\mu_p = 5$, $k_{max} = 12$. Error bands are statistical and uncorrelated systematic only.

FIG. 7.   Extracted electric (top panel) and magnetic (bottom panel) radii as functions of the kinematic cut Q^2_{max} on momentum transfer for the world cross section data set, using the z expansion with $t_0 = 0$, Gaussian priors with $|a_k|_{max} = |b_k|_{max}/\mu_p = 5$, $k_{max} = 12$. Error bands include statistical and systematic uncertainties.

world data. However, this approach allows the correlated systematic corrections to be different for each subset, which may not be significantly better than the assumption in the Mainz analysis that these corrections are identical for different subsets. We thus present separate fits to the Mainz and world data sets so that the comparison can be made without worrying about how to consistently treat Mainz and world uncertainties.

For the analysis of world data, we take the χ^2 function

$$\chi^2_w = \chi^2_\sigma + \chi^2_b + \chi^2_n. \qquad (36)$$

Here, χ^2_σ and χ^2_b are identical to those used for the Mainz analysis, Eqs. (32) and (33). Because these experiments provide a normalization uncertainty, we follow previous analyses and include χ^2_n for the floating normalization parameters assigned to each experiment, where

$$\chi^2_n = \sum_{i=1}^{N_{exp}} \frac{(1 - \eta_{i,fit})^2}{d\eta_i^2}. \qquad (37)$$

Below $Q^2 = 1$ GeV^2, there are $N_{exp} = 23$ independent experiments, and $d\eta_i$ ranges from 1.5% to 4.6%. For the fit to the combined world and polarization data sets, we include an additional term for the recoil polarization and polarized target measurements of $\mu_p G_E/G_M$,

$$\chi^2_{w+p} = \chi^2_w + \sum_{i=1}^{N_{rat}} \frac{(R_i - R_{i,fit})^2}{dR_i^2}, \qquad (38)$$

where $R_i = \mu_p G_E(q_i^2)/G_M(q_i^2)$.

The TPE model for the cross section data in these analyses is the SIFF prescription with the form factor as a sum of monopoles from Table I.[19] As in the fit to the A1 MAMI data set, we find little difference in the r_E results using either a dipole form factor or the Feshbach correction but significant differences in the r_M results between approaches. For $Q^2_{max} = 1$ GeV^2, there are $N_\sigma = 363$ cross section data points, $N_{rat} = 41$ polarization data points, and $N_{exp} = 23$ normalization parameters. Results for fits using the z expansion with our default $t_0 = 0$, $k_{max} = 12$, and Gaussian bounds $|a_k|_{max} = |b_k|_{max}/\mu_p = 5$, are displayed in Figs. 7 and 8. Table XI contains the radii values and error budget for particular values of Q^2_{max}. The results in Table XI indicate that the inclusion of the polarization data does not significantly change the extracted radii. The results for the electric radius are in agreement with the fit to the Mainz data in Table X, while magnetic radius values disagree by 2.7σ if the uncertainties are added in quadrature.

---

[19]The use of different conventions in the world data to isolate the IR finite TPE contribution, as detailed after Eq. (23), changes r_E and r_M by less than 0.003 fm.
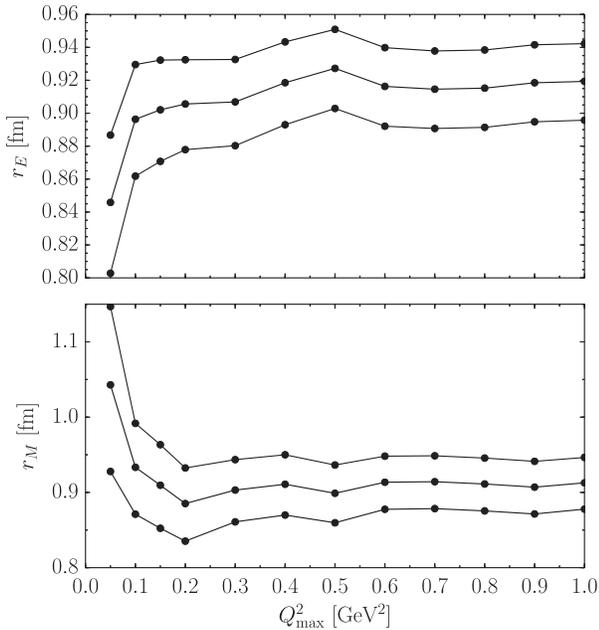
FIG. 8.   Same as Fig. 7 but with both the world polarization data in addition to the world cross section data.

C. Consistency checks

We have derived best-fit values for r_E and r_M from the Mainz data set and from a world data set excluding the Mainz data. We observe a significant dependence of the Mainz radius on the Q^2 range included in the fit as well as a disagreement between the Mainz and world data extractions of r_M. Here, we describe several consistency checks on the fits we have performed. We also consider the possibility of a common systematic not specific to a particular experiment and reexamine subleading radiative corrections which become enhanced at large Q^2.

1. Priors

Let us revisit the dependence on the class of form factors over which the fit is performed, defined in the bounded z expansion by the choice of k_{max}, t_0, and coefficient bound.

As discussed above in Sec. V D 1, we have taken k_{max} large enough such that the fit results are independent of the precise value of k_{max}, removing this choice from the discussion of prior dependence.

TABLE XI.   Final radius results from the fits to the world cross section data in Fig. 7 (first line) and to the combined world cross section and polarization data in Fig. 8 (second line). There is no polarization data below $Q^2 = 0.05$ GeV^2.

Q^2_{max} (GeV^2)	r_E (fm)	r_M (fm)	χ^2	N_σ	N_{rat}	N_{exp}
0.05	0.846(42)	1.04(11)	52.9	111	0	8
0.5	0.910(25)	0.919(38)	163.4	269	0	15
	0.927(24)	0.899(38)	234.5	269	30	15
1	0.916(24)	0.914(34)	260.9	363	0	23
	0.919(23)	0.913(34)	366.0	363	41	23

With our imposition of coefficient bounds, the chosen form factor class depends on t_0.[20] We have redone selected fits with different scheme choices, e.g., $t_0 = t_0^{opt}$ defined after Eq. (8), finding negligible dependence on t_0 in the large k_{max} limit.

Regarding Gaussian vs sharp priors, we have employed Gaussian priors for numerical ease but have checked that our results are not significantly changed if sharp priors are used. Central values for both r_E and r_M differ by a negligible amount between the two priors, and the difference in radius errors is small.

We note that enforcing a bound on the radius parameters could in principle bias the radius fits. For example, at $t_0 = 0$ (or default choice), the squared radii are proportional to fit parameters a_1 and b_1, and a bound on these parameters would tend to bias fits toward smaller radii. We have checked that fitting with the bounds on a_1 and b_1 removed has a negligible impact.

Finally, consider the choice of the numerical value for the bound. We choose a Gaussian bound of 5, i.e., $|a_k/a_0|_{max} = |b_k/b_0|_{max} = 5$, for our fits, based on the sum rules and studies discussed in Sec. III B. Our implementation of the bounds is meant to be very conservative, especially at large k, where the coefficients must fall as $1/k^4$. We examined the impact of tightening the constraint for larger values of k, taking a bound of 5 for $k = 1, ..., 4$ and a bound of $20/k$ for larger k values. This yields small changes in the central radius values ($< 0.3\sigma$), with only slightly smaller uncertainties. Because tighter high-k constraints have a minimal impact, for simplicity, we use a fixed bound of $|a_k/a_0|_{max} = |b_k/b_0|_{max} = 5$. More aggressive priors or k_{max} truncations could be invoked to reduce the statistical/fit uncertainty on the radius at the expense of introducing model-dependent truncation errors. This may allow for the possibility of reduced uncertainties in the extracted radii, if one can verify that the reduction in uncertainty coming from tighter bounds or truncations is not replaced with a bias that yields a larger net uncertainty. In this work, we are focused on minimizing any such biases and so do not attempt to further constrain the fits.

We also fit the data and obtained statistical errors for larger bounds, $|a_k/a_0|_{max} = |b_k/b_0|_{max} = 10$. The change in the extracted radii is very small for fits with large k_{max} (in particular for our default $k_{max} = 12$). No additional uncertainty is applied as typical changes in the fit were significantly smaller than the statistical or the correlated systematic uncertainties. Fits in which k_{max} was not sufficiently large to give fully converged results showed larger changes but are not included in the final results presented here.

---

[20]Modifications (multiplication by suitable analytic function ϕ) to the z expansion can ensure that the form factor class is rigorously independent of t_0 in the large k_{max} limit if the bound is placed on $\sum_k a_k^2$. See, e.g., Ref. [75].

2. Data set exclusions

To verify that the fits to the Mainz data set are not biased by one particular subset of the data, we redo our best fits for r_E and r_M 18 times, excluding in each fit a particular energy/spectrometer combination. The results are displayed in Tables XII and XIII for $Q^2_{max} = 0.5$ and 1 GeV^2, respectively. For the electric radius, the impact of each subset exclusion is typically less than half of the total statistical error (taken from Table X). Several subset exclusions impact the magnetic radius at a level comparable to or greater than the total statistical error. For the 180 MeV data, excluding any one of the three spectrometers gives a 0.030–0.041 fm shift in r_M. This is much larger than the estimated systematic uncertainty and much larger than one might expect based on an exclusion of 4%–11% of the data points. While this suggests the need for a larger uncertainty in the quoted value of r_M, it is hard to quantify what uncertainty would be appropriate as we are comparing highly correlated fits. As such, we simply note this as another potential issue, similar to the anomalous Q^2_{max} dependence observed in the extraction of the charge radius.

3. Subleading radiative corrections

We have used standard prescriptions for the electron vertex and bremsstrahlung radiative corrections. As noted above, in the $Q^2 \sim$ GeV^2 regime, it is critical to resum the leading $\alpha \log^2(Q^2/m_e^2)$ terms. However, numerically enhanced subleading logarithms can also have a significant impact, as illustrated by the following considerations. This

TABLE XII. Change in extracted r_E and r_M when each data subset is excluded. Fits are for rebinned A1 MAMI data set with 0.3%–0.4% uncorrelated systematic uncertainties at $Q^2_{max} = 0.5$ GeV^2 (568 data points), using the z expansion with $t_0 = 0$, Gaussian priors with $|a_k|_{max} = |b_k|_{max}/\mu_p = 5$, $k_{max} = 12$.

Spec.	Beam	N_σ	Δr_E(fm)	Δr_M(fm)
A	180	539	−0.008	−0.031
	315	545	+0.001	−0.008
	450	543	−0.004	+0.008
	585	540	0.000	−0.009
	720	552	−0.003	−0.002
	855	561	0.000	0.000
B	180	507	−0.001	+0.034
	315	522	+0.001	+0.003
	450	500	+0.003	−0.017
	585	508	+0.005	+0.005
	720	511	−0.002	−0.006
	855	502	+0.005	+0.019
C	180	544	−0.002	+0.030
	315	544	0.000	−0.023
	450	543	−0.006	+0.032
	585	561	−0.001	+0.001
	720	566	0.000	0.000
	855	568	—	—

TABLE XIII. Same as Table XII, but for $Q^2_{max} = 1$ GeV^2 (657 data points).

Spec.	Beam	N_σ	Δr_E(fm)	Δr_M(fm)
A	180	628	−0.008	−0.035
	315	634	−0.001	−0.007
	450	632	−0.004	+0.012
	585	629	−0.002	−0.015
	720	628	−0.004	−0.003
	855	636	−0.001	−0.004
B	180	596	0.000	+0.041
	315	611	0.000	+0.004
	450	589	+0.004	−0.016
	585	597	+0.005	+0.006
	720	600	−0.004	−0.007
	855	591	+0.007	+0.020
C	180	633	−0.003	+0.036
	315	633	+0.001	−0.017
	450	632	−0.006	+0.021
	585	639	+0.001	−0.000
	720	625	−0.002	−0.005
	855	636	+0.001	+0.001

exercise is presented both as an illustration of how a correction would need to deviate from the assumptions of Sec. VI C 4 in order to reconcile muonic hydrogen with electron scattering measurements of the charge radius and to point out the potential impact of a class of naively subleading but numerically enhanced radiative corrections.

Recall the explicit form for the sum of the one-loop electron vertex and real bremsstrahlung radiative corrections,

$$\delta = \frac{\alpha}{\pi} \left\{ \left[\log \frac{Q^2}{m_e^2} - 1 \right] \log \frac{(\eta \Delta E)^2}{EE'} + \frac{13}{6} \log \frac{Q^2}{m_e^2} + \cdots \right\},$$

(39)

where $\eta = E/E'$ and the ellipsis denotes terms not containing large logarithms. In the regime where $\Delta E \sim m_e$ (and $E \sim E' \sim Q$), the numerically relevant leading log term

$$\delta = \frac{\alpha}{\pi} \left\{ -\log^2 \frac{Q^2}{m_e^2} + \cdots \right\}$$

(40)

is fixed by infrared divergences whose forms are dictated by soft photon theorems [76]. Equivalently, an effective theory renormalization analysis between hard ($\sim Q$) and soft ($\sim m_e$) scales determines the relevant Sudakov form factor. However, in practice, ΔE can be large compared to m_e, introducing another scale into the problem, and associated large logarithms not captured by the naive exponentiation of one-loop corrections. A complete analysis is outside the scope of the present paper, but to illustrate the potential impact, let us consider in place of the ansatz that makes the replacement (31) in Eq. (29) the following expressions:
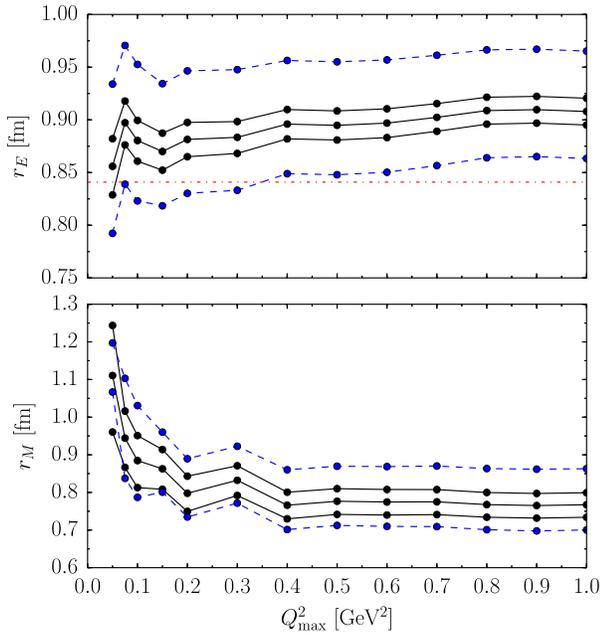
FIG. 9 (color online). Illustrative fit with modified radiative corrections given by Eq. (41) using $\Delta E = 10$ MeV. Lower and upper dashed blue lines correspond to the plus sign and minus sign in Eq. (41), respectively. Fits are for the 657 point rebinned A1 MAMI data set with 0.3%–0.4% uncorrelated systematic uncertainties using the z expansion with $t_0 = 0$, Gaussian priors with $|a_k|_{max} = |b_k|_{max}/\mu_p = 5$, $k_{max} = 12$. Black solid lines reproduce the curves in Fig. 6. For orientation, the dash-dotted red line indicates the muonic hydrogen value for r_E.

$$(1 + \delta) \rightarrow \left[1 \pm \left(\delta + \frac{\alpha}{\pi}\log^2\frac{Q^2}{m_e^2}\right)\right]^{\pm 1} \exp\left(-\frac{\alpha}{\pi}\log^2\frac{Q^2}{m_e^2}\right).$$
(41)

These expressions agree with the known corrections through one-loop order and resum the leading logarithms to all orders in perturbation theory when there is only one large ratio of scales.

Figure 9 illustrates the impact of applying the correction on the right-hand side of Eq. (41) in place of the ansatz (31). For definiteness, the plot takes $\Delta E = 10$ MeV. As indicated in the figure, the shifts in the radii under this correction are a factor $\sim$2–3 larger than those allowed in Table IX, which considered corrections varying by 0.5% over beam-energy/spectrometer combinations. The variation of the correction (41) over beam-energy/spectrometer combinations [i.e., the magnitude of a in Eq. (35)] ranges between 0.9% and 2.6%, with an average 1.5%.

D. Final radius extractions

A global analysis combining Mainz and other world data will artificially favor the Mainz data, as the uncertainties associated with each cross section measurement include only a small part of the total uncertainty. Thus, we provide best-fit values separately for our analyses of the Mainz and
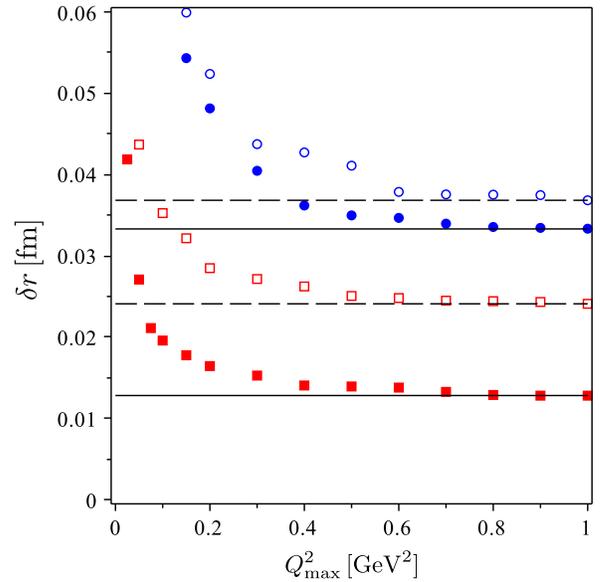
FIG. 10 (color online).   Statistical error on r_E (bottom, red squares) and r_M (top, blue circles) as a function of Q^2_{max}. Solid symbols are for the 1422 point A1 MAMI data set, and open symbols are for the world cross section and polarization data set. Fits use the z expansion with $t_0 = 0$, Gaussian priors with $|a_k|_{max} = |b_k|_{max}/\mu_p = 5$, $k_{max} = 12$.

world data. To determine an optimal Q^2_{max}, Fig. 10 illustrates the statistical uncertainty on r_E and r_M found using our default fit both to the 1422 point Mainz data set and to the world data set. For the Mainz data, the uncertainty is minimized by taking $Q^2_{max} \gtrsim 0.5$ GeV^2, with negligible improvement beyond this point. To maximize the statistical power of the data, while minimizing potential systematic effects in higher Q^2 data, we take for definiteness the $Q^2_{max} = 0.5$ GeV^2 results of the previous sections.[21]

We then have for the Mainz data set, from Table X,

$$r_E^{Mainz} = 0.895(14)(14), \qquad r_M^{Mainz} = 0.776(34)(17),$$
(42)

where the first error comes from counting statistics and uncorrelated systematics and the second error comes from variation of the bremsstrahlung energy cut and correlated systematics. For the world data set, including cross section and polarization measurements, we take a slightly higher $Q^2_{max} = 0.6$ GeV^2 based on Fig. 10. We then have

$$r_E^{world} = 0.916(24), \qquad r_M^{world} = 0.914(35). \quad (43)$$

---

[21]A similar choice was made in Ref. [16] based on radius sensitivity in the world data summarized by extracted form factors [26]. Related argumentation for the Q^2_{max} dependence of radius sensitivity, based on continued-fraction expansion, is given in Ref. [27].

These values correspond to the same analysis as presented in Table XI, but for a fit with $Q^2_{max} = 0.6$ GeV^2. In contrast to the Mainz data, the world data have combined statistical and systematic uncertainties at the cross section level and so have only a single combined uncertainty.

The electric charge radius results are consistent with each other and between one and two standard deviations higher than the atomic physics measurements based on atomic hydrogen which yield $r_E = 0.8758(77)$ fm [1]. They are well above the muonic hydrogen result $r_E = 0.84087(39)$ fm [4]. The magnetic radii differ significantly, indicating an unresolved tension between the Mainz data set and the world data set.

A simple combination of the results (42) and (43) yields

$$r_E^{avg} = 0.904(15), \qquad r_M^{avg} = 0.851(26). \qquad (44)$$

While the Mainz and world data sets have comparable total uncertainties, the high statistics of the Mainz data set imply that in this case the errors are dominantly systematic. It is not entirely clear that a simple average of the Mainz and world results is appropriate [11,15]. The magnetic radii differ by 2.7σ, suggesting an inconsistency between Mainz and world cross sections that is ignored in averaging the results. In addition, the simple combination assumes that the uncertainties for the Mainz and world data analyses are independent, which may not be the case if there is a common error, e.g., due to approximations in the radiative correction procedures.

VIII. SUMMARY AND DISCUSSION

We have performed a comprehensive analysis of electron-proton scattering data to determine the proton electric and magnetic radii. Our analysis incorporates constraints of analyticity and perturbative scaling which enforce model-independent bounds on form factor shape. The bounded z expansion ensures that the true form factor is guaranteed to lie within the space of considered curves, while at the same time being sufficiently restrictive to enable meaningful radius extractions. We focused on the high-statistics Mainz data set and performed a wide-ranging study of the impact of potential systematic errors. We discussed potential flaws in the procedure of rescaling statistical errors and addressed these by rebinning data taken at identical kinematic settings and applying a constant uncorrelated systematic error that is not assumed to scale with statistics. We also reevaluated the correlated systematic uncertainties, increasing the size of these effects to include contributions neglected in the original analysis and examining different approaches to evaluating the impact of such corrections on the radius.

Table XIV displays the progression of results leading up to the final Mainz radius values, as various improvements are included in the analysis. The data exhibit several issues that suggest the need for additional uncertainties but for which it is difficult to quantify an appropriate correction or

TABLE XIV. Charge and magnetic radii as determined in Ref. [9] compared to the sequence of fits leading to the final values determined in this paper. For the Mainz data set, the first error is a combination of statistics and uncorrelated systematics, and the second error is from correlated systematics. The entry labeled "alternate approach" is the test from Sec. VI C 3 which evaluates the impact of the correlated systematic uncertainties as part of the fit, rather than evaluating it separately.

	Source	r_E (fm)	r_M (fm)
A1 spline	[9]	0.879(5)(10)	0.777(13)(14)
Bounded z exp.	Tab. III	0.920(9)(-)	0.743(25)(-)
+Hadronic TPE	Tab. IV	0.918(9)(-)	0.780(25)(-)
Rebin, 0.3%–0.4% syst.	Tab. X	0.908(13)(-)	0.767(33)(-)
+0.4% corr. syst.	Tab. X	0.908(13)(14)	0.767(33)(22)
$Q^2_{max} = 0.5$ GeV^2	(42)	0.895(14)(14)	0.776(34)(17)
(Alternate approach)	VI C 3	0.891(18)(-)	0.792(49)(-)
New fit to world data	(43)	0.916(24)	0.914(35)
Simple avg.	(44)	0.904(15)	0.851(26)

uncertainty contribution. There is an unusually large variation of r_E and r_M with the Q^2 range included in the fit, as illustrated in Fig. 6. In addition, the exclusion of individual data sets, in particular at low beam energy, has an unusually large impact on the extracted radii. Despite these anomalous features, inclusion of the above improvements leads to a proton charge radius that is larger than extracted in the original A1 analysis [9] and, even with the larger uncertainty, almost 3σ above the value $r_E \approx 0.84$ fm inferred from muonic hydrogen. Based on our examination of the systematic uncertainties, resolving this discrepancy would require correlated systematic effects well above the 0.5% level that was considered in our analysis.

As an independent check of the radius, we performed the analogous fit to the world data excluding Mainz data. The systematic error treatment in the world data set differs in that the systematic errors are included in each cross section data point as opposed to deduced from a combination of statistics rescaling and model-dependent correlated systematics analysis. It is thus not straightforward to perform a meaningful combined fit, but observables such as radius values may be compared to verify consistency. In this comparison, the Mainz and world r_E values are in good agreement, and the r_M values differ by 2.7σ. This is perhaps not surprising, given the clear disagreement between the Mainz form factors and world data, in particular for G_M at low Q^2 [9]. Putting aside the discrepancy in magnetic radii, the charge radius puzzle persists, with the world value for r_E 3σ high compared to muonic hydrogen and the combined Mainz + world average discrepant at the 4.2σ level. In light of this, it is also important to inquire to what extent an underestimated systematic effect or theoretical correction could be common to both data sets.

The theoretical input to the radius extraction consists of specifying the form factor class and defining the radiative correction model. We have examined in detail

the uncertainties associated with form factor shape assumptions. We find a large impact from fitting to the physical form factor class defined by the bounded z expansion, compared to polynomial or inverse polynomial fits. Somewhat surprisingly, the central value for the charge radius goes in the direction of *increasing* tension between the electron scattering and muonic hydrogen. We have further examined the dependence of radius values on form factor priors, finding that such a residual dependence is small compared to other uncertainties.

The other theoretical input is the radiative correction model, as described in Sec. IV. For the most part, the corrections are known precisely or, for model-dependent terms including hadronic vacuum polarization or proton vertex corrections, the uncertainties are estimated to be small compared to the uncertainty in the radius extraction. Through one-loop order, the only essential model dependence of the radiative corrections enters from the description of the TPE. Varying over models in the literature reveals no large dependence on the applied TPE correction. The $Q^2 \sim$ GeV^2 regime demands QED radiative corrections beyond one-loop order. In the counting $m_e \sim \Delta E$, leading logarithms are resummed by a standard ansatz. Subleading logarithms then enter at a level expected to be contained within the 0.4% systematic error budget. Possible enhancements, either simply numerical or due to the hierarchy $\Delta E \gg m_e$, could potentially give rise to larger effects. The Mainz and world data sets differ in their treatment of bremsstrahlung radiation and approximations based on (31) and in the uncertainties ascribed to these effects. More refined calculations, including a detailed examination of experimental conditions and the interplay with background modeling and subtraction, are required in order to fully address this question [77].

Further constraints may be placed on the proton form factors in combination with electron-proton scattering data. In particular, the inclusion of either electron-neutron scattering data, or both electron-neutron and pion-nucleon data, allows the threshold t_{cut} appearing in the definition of the z expansion (8) for the isoscalar/isovector decomposition of the form factors to be raised from $4m_\pi^2$ to either $9m_\pi^2$ or $16m_\pi^2$. This yields a smaller $|z|_{\text{max}}$ and hence tighter constraints on the form factors and smaller radius uncertainties. Isospin violating corrections and systematic uncertainties in the additional data must be properly accounted for. These additional constraints by themselves cannot offer a satisfactory resolution to the proton radius puzzle, since they would then be inconsistent with the results of the fit to the electron scattering data alone. Similar remarks hold for the model spectral function analysis in Ref. [78]. We note that it is not feasible to reconstruct accurate spectral functions for form factors, Im$G(t)$, from scattering data, since these have support at $|z| = 1$.

Electron scattering data from a polarized target have been taken and will provide low-Q^2 measurements of $\mu_p G_E/G_M$, down to $Q^2 \approx 0.02$ GeV^2, yielding a more sensitive measurement of the magnetic form factor in this region [79]. Future experiments will obtain low-Q^2 ($\sim 10^{-4}$–10^{-2} GeV^2) proton form factor measurements less prone to high-Q^2 systematics [80,81]. Muon-proton scattering promises to provide further insight [82]. Independent of scattering measurements, new results are anticipated from hydrogen spectroscopy that may impact the charge radius discrepancy, including a new microwave measurement of the 2S-2P Lamb shift [83], measurement of 2S-4P transitions [84], and 1S-3S/3D transitions [85,86]. Next-generation lattice QCD simulations may provide another handle [87–91]; in particular, resolving the $\sim$8% discrepancy between $r_E \approx 0.84$ fm of muonic hydrogen and $r_E \approx 0.91$ fm of the simple fit to Mainz electron scattering data is a viable present-day target. Such first-principles calculations would be independent of radiative corrections involving the electron, thus avoiding the reliance on hadronic models for TPE, and detector-dependent modeling of radiative tails.

Regardless of its resolution, the proton radius puzzle has important implications across particle, nuclear, and atomic physics. For example, understanding and controlling systematic effects, including radiative corrections, at the percent level will be critical for measurements at future long baseline neutrino experiments [92]. Any deficiency in the theoretical treatment of electron-proton scattering will be exacerbated in neutrino applications by the presence of additional flux uncertainties and nuclear corrections. Much more intriguing is the possibility that updated measurements and a detailed examination of the radiative corrections will not resolve the discrepancy. Already much work has been performed to find explanations in terms of physics beyond the Standard Model [7,8,93–98]. Future measurements will provide more stringent tests of the discrepancy in electron scattering and atomic hydrogen, with plans to directly compare electron-proton and muon-proton scattering as a test of lepton nonuniversality.

[1] P. J. Mohr, B. N. Taylor, and D. B. Newell, Rev. Mod. Phys. **84**, 1527 (2012).

[2] A. de Gouvea et al. (Intensity Frontier Neutrino Working Group Collaboration), arXiv:1310.4340.

[3] R. Pohl et al., Nature (London) **466**, 213 (2010).

[4] A. Antognini et al., Science **339**, 417 (2013).

[5] B. Bhattacharya, R. J. Hill, and G. Paz, Phys. Rev. D **84**, 073006 (2011).

[6] M. Day and K. S. McFarland, Phys. Rev. D **86**, 053003 (2012).

[7] R. Pohl, R. Gilman, G. A. Miller, and K. Pachucki, Annu. Rev. Nucl. Part. Sci. **63**, 175 (2013).

[8] C. E. Carlson, Prog. Part. Nucl. Phys. **82**, 59 (2015).

[9] J. C. Bernauer et al. (A1 Collaboration), Phys. Rev. C **90**, 015206 (2014).

[10] M. Distler (private communication).

[11] J. Arrington, J. Phys. Chem. Ref. Data **44**, 031203 (2015).

[12] J. Arrington, Phys. Rev. Lett. **107**, 119101 (2011).

[13] X. Zhan et al., Phys. Lett. B **705**, 59 (2011).

[14] I. Sick, Prog. Part. Nucl. Phys. **67**, 473 (2012).

[15] J. Arrington and I. Sick, J. Phys. Chem. Ref. Data **44**, 031204 (2015).

[16] R. J. Hill and G. Paz, Phys. Rev. D **82**, 113005 (2010).

[17] Z. Epstein, G. Paz, and J. Roy, Phys. Rev. D **90**, 074027 (2014).

[18] M. A. Belushkin, H.-W. Hammer, and U.-G. Meissner, Phys. Rev. C **75**, 035202 (2007).

[19] See Supplemental Material at http://link.aps.org/supplemental/10.1103/PhysRevD.92.013013 for the compilations of Mainz and world cross section data and world polarization data used in this analysis.

[20] K. Nakamura et al. (Particle Data Group), J. Phys. G **37**, 075021 (2010).

[21] For a review and further references, see R. J. Hill, Proceedings of 4th Flavor Physics and CP Violation Conference (FPCP 2006), Vancouver, 2006, eConf C060409, 027 (2006).

[22] G. P. Lepage and S. J. Brodsky, Phys. Rev. D **22**, 2157 (1980).

[23] A. Ahmadi, A. Olshevsky, P. A. Parrilo, and J. N. Tsitsiklis, Math. Program. **137**, 453 (2013).

[24] J. Arrington, Phys. Rev. C **69**, 022201 (2004).

[25] J. J. Kelly, Phys. Rev. C **70**, 068202 (2004).

[26] J. Arrington, W. Melnitchouk, and J. A. Tjon, Phys. Rev. C **76**, 035205 (2007).

[27] I. Sick, Phys. Lett. B **576**, 62 (2003).

[28] J. Arrington and I. Sick, Phys. Rev. C **76**, 035201 (2007).

[29] Y.-S. Tsai, Phys. Rev. **122**, 1898 (1961).

[30] L. C. Maximon and J. A. Tjon, Phys. Rev. C **62**, 054320 (2000).

[31] R. Ent, B. W. Filippone, N. C. R. Makins, R. G. Milner, T. G. O'Neill, and D. A. Wasson, Phys. Rev. C **64**, 054610 (2001).

[32] R. J. Hill and G. Paz, Phys. Rev. Lett. **107**, 160402 (2011).

[33] F. Jegerlehner, Nucl. Phys. B, Proc. Suppl. **51C**, 131 (1996).

[34] J. L. Friar, J. Martorell, and D. W. L. Sprung, Phys. Rev. A **59**, 4061 (1999).

[35] P. G. Blunden, W. Melnitchouk, and J. A. Tjon, Phys. Rev. C **72**, 034612 (2005).

[36] P. G. Blunden, W. Melnitchouk, and J. A. Tjon, Phys. Rev. Lett. **91**, 142304 (2003).

[37] C. E. Carlson and M. Vanderhaeghen, Annu. Rev. Nucl. Part. Sci. **57**, 171 (2007).

[38] J. Arrington, P. G. Blunden, and W. Melnitchouk, Prog. Part. Nucl. Phys. **66**, 782 (2011).

[39] W. A. McKinley and H. Feshbach, Phys. Rev. **74**, 1759 (1948).

[40] M. Vanderhaeghen, J. M. Friedrich, D. Lhuillier, D. Marchand, L. Van Hoorebeke, and J. Van de Wiele, Phys. Rev. C **62**, 025501 (2000).

[41] L. W. Mo and Y. S. Tsai, Rev. Mod. Phys. **41**, 205 (1969).

[42] Y. S. Tsai, Report No. SLAC-PUB-0848; Report No. SLAC-PUB-848.

[43] R. C. Walker et al., Phys. Rev. D **49**, 5671 (1994).

[44] J. Arrington, Phys. Rev. C **69**, 032201 (2004).

[45] D. Frerejacque, D. Benaksas, and D. J. Drickey, Phys. Rev. **141**, 1308 (1966).

[46] D. Ganichot, B. Grossetete, and D. B. Isabelle, Nucl. Phys. **A178**, 545 (1972).

[47] I. A. Qattan et al., Phys. Rev. Lett. **94**, 142301 (2005).

[48] M. E. Christy et al. (E94110 Collaboration), Phys. Rev. C **70**, 015206 (2004).

[49] B. D. Milbrath et al. (Bates FPP Collaboration), Phys. Rev. Lett. **80**, 452 (1998); **82**, 2221 (1999).

[50] O. Gayou et al., Phys. Rev. C **64**, 038202 (2001).

[51] T. Pospischil et al. (A1 Collaboration), Eur. Phys. J. A **12**, 125 (2001).

[52] S. Strauch et al. (Jefferson Lab E93-049 Collaboration), Phys. Rev. Lett. **91**, 052301 (2003).

[53] G. MacLachlan et al., Nucl. Phys. **A764**, 261 (2006).

[54] M. K. Jones et al. (Resonance Spin Structure Collaboration), Phys. Rev. C **74**, 035201 (2006).

[55] C. B. Crawford et al., Phys. Rev. Lett. **98**, 052301 (2007).

[56] A. J. R. Puckett et al., Phys. Rev. Lett. **104**, 242301 (2010).

[57] M. K. Jones et al. (Jefferson Lab Hall A Collaboration), Phys. Rev. Lett. **84**, 1398 (2000).

[58] O. Gayou et al. (Jefferson Lab Hall A Collaboration), Phys. Rev. Lett. **88**, 092301 (2002).

[59] G. Ron et al., Phys. Rev. Lett. **99**, 202002 (2007).

[60] V. Punjabi et al., Phys. Rev. C **71**, 055202 (2005); **71**, 069902(E) (2005).

[61] A. J. R. Puckett et al., Phys. Rev. C **85**, 045203 (2012).

[62] G. Ron et al. (Jefferson Lab Hall A Collaboration), Phys. Rev. C **84**, 055204 (2011).

[63] J. Arrington, Phys. Rev. C **68**, 034325 (2003).

[64] M. Goitein, R. J. Budnitz, L. Carroll, J. R. Chen, J. R. Dunning, K. Hanson, D. C. Imrie, C. Mistretta, and R. Wilson, Phys. Rev. D **1**, 2449 (1970).

[65] W. Bartel, F.-W. Büsser, W.-R. Dix, R. Felst, D. Harms, H. Krehbiel, P. E. Kuhlmann, J. McElroy, J. Meyer, and G. Weber, Nucl. Phys. **B58**, 429 (1973).

[66] L. Andivahis et al., Phys. Rev. D **50**, 5491 (1994).

[67] J. Arrington, J. Phys. G **40**, 115003 (2013).

[68] G. G. Simon, C. Schmitt, F. Borkowski, and V. H. Walther, Nucl. Phys. **A333**, 381 (1980).

[69] G. P. Lepage, B. Clark, C. T. H. Davies, K. Hornbostel, P. B. Mackenzie, C. Morningstar, and H. Trottier, Nucl. Phys. B, Proc. Suppl. **106–107**, 12 (2002).

[70] M. R. Schindler and D. R. Phillips, Ann. Phys. (Amsterdam) 324, 682 (2009); 324, 2051(E) (2009).

[71] E. Kraus, K. E. Mesick, A. White, R. Gilman, and S. Strauch, Phys. Rev. C 90, 045206 (2014).

[72] I. T. Lorenz and U. G. Meiner, Phys. Lett. B 737, 57 (2014).

[73] D. Adikaram et al. (CLAS Collaboration), Phys. Rev. Lett. 114, 062003 (2015).

[74] I. A. Rachek et al., Phys. Rev. Lett. 114, 062005 (2015).

[75] T. Becher and R. J. Hill, Phys. Lett. B 633, 61 (2006).

[76] D. R. Yennie, S. C. Frautschi, and H. Suura, Ann. Phys. (N.Y.) 13, 379 (1961).

[77] R. J. Hill (unpublished).

[78] I. T. Lorenz, U. G. Meiner, H.-W. Hammer, and Y.-B. Dong, Phys. Rev. D 91, 014023 (2015).

[79] J. Arrington, D. Day, R. Gilman, D. Higinbotham, G. Ron, and A. Sarty, Jefferson Lab experiment Report No. E08-007, https://www.jlab.org/exp_prog/generated/apphalla.html.

[80] A. Gasparian (PRad at JLab Collaboration), Eur. Phys. J. Web Conf. 73, 07006 (2014).

[81] M. Mihovilovic et al. (A1 Collaboration), Eur. Phys. J. Web Conf. 72, 00017 (2014).

[82] R. Gilman et al. (MUSE Collaboration), arXiv:1303.2160.

[83] A. Vutha et al., Report No. BAPS.2012.DAMOP.D1.138, 2012.

[84] A. Beyer et al., J. Phys. Conf. Ser. 467, 012003 (2013).

[85] O. Arnoult, F. Nez, L. Julien, and F. Biraben, Eur. Phys. J. D 60, 243 (2010).

[86] E. Peters, D. C. Yost, A. Matveev, T. W. Hänsch, and T. Udem, Ann. Phys. (Amsterdam) 525, L29 (2013).

[87] T. Yamazaki, Y. Aoki, T. Blum, H. W. Lin, S. Ohta, S. Sasaki, R. Tweedie, and J. Zanotti, Phys. Rev. D 79, 114505 (2009).

[88] J. D. Bratt et al. (LHPC Collaboration), Phys. Rev. D 82, 094502 (2010).

[89] C. Alexandrou, M. Constantinou, S. Dinter, V. Drach, K. Jansen, C. Kallidonis, and G. Koutsou, Phys. Rev. D 88, 014509 (2013).

[90] T. Bhattacharya, S. D. Cohen, R. Gupta, A. Joseph, H. W. Lin, and B. Yoon, Phys. Rev. D 89, 094502 (2014).

[91] J. R. Green, J. W. Negele, A. V. Pochinsky, S. N. Syritsyn, M. Engelhardt, and S. Krieg, Phys. Rev. D 90, 074507 (2014).

[92] C. Adams et al. (LBNE Collaboration), arXiv:1307.7335.

[93] V. Barger, C. W. Chiang, W. Y. Keung, and D. Marfatia, Phys. Rev. Lett. 106, 153001 (2011).

[94] D. Tucker-Smith and I. Yavin, Phys. Rev. D 83, 101702 (2011).

[95] B. Batell, D. McKeen, and M. Pospelov, Phys. Rev. Lett. 107, 011803 (2011).

[96] E. Izaguirre, G. Krnjaic, and M. Pospelov, Phys. Lett. B 740, 61 (2015).

[97] V. Pauk and M. Vanderhaeghen, arXiv:1503.01362.

[98] C. E. Carlson and M. Freid, arXiv:1506.06631.